

Applied Surface Science

Multi-functional oxidase-like activity of praseodymia nanorods and nanoparticles

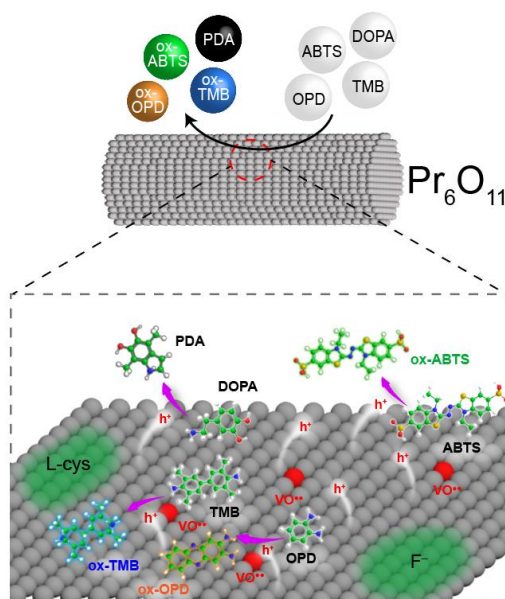
--Manuscript Draft--

Manuscript Number:	APSUSC-D-22-10755R2
Article Type:	Full Length Article
Keywords:	praseodymia; Nanorods; nanoparticles; artificial enzyme; oxidase
Corresponding Author:	Xiaowei Chen, Ph.D. University of Cadiz Puerto Real, Cadiz SPAIN
First Author:	Lei Jiang, Ph.D.
Order of Authors:	Lei Jiang, Ph.D. Yaning Han Susana Fernández-García, Ph.D. Miguel Tinoco, Ph.D. Zhuang Li Pengli Nan Jingtao Sun Juan Delgado, Ph.D. Huiyan Pan, Ph.D. Ginesa Blanco, Ph.D. Javier Martínez-López, Ph.D. Ana Hungria, Ph.D. Jose Calvino, Ph.D. Xiaowei Chen, Ph.D.
Abstract:	<p>The ability to mimic protein-based oxidase with multi-functional inorganic nanozymes would greatly advance biomedical and clinical practices. Praseodymia (PrO_x) nanorods (NRs) and nanoparticles (NPs) have been synthesized using hydrothermal and precipitation methods. Both PrO_x catalysts with different morphologies exhibit significantly higher oxidase-like activities (Michaelis-Menten constant $K_m \approx 0.026$ mM) than commercial PrO_x and most so-far-reported artificial enzymes. One of the substrates, dopamine, can be oxidized and further polymerized to generate polydopamine in acidic conditions. Akin to CeO₂, which is a well-studied nanozyme, a different mechanism involving holes + , oxygen vacancies and oxygen mobility over PrO_x catalysts has been proposed in this work. However, fluoride ions were found to impose opposite effects on the oxidase-mimicking activity of PrO_x and CeO₂, implying a promising path for the exploration of new nanozymes. In support of this, PrO_x was further applied in colorimetric sensing of L-cysteine and fluoride with high sensitivity.</p>
Suggested Reviewers:	<p>Mengfei Luo, PhD Zhejiang Normal University mengfeiluo@zjnu.cn Professor Luo has been working on lanthanide-based catalysts for a long time.</p> <p>Mingyuan Zheng, PhD Dalian Institute of Chemical Physics Chinese Academy of Sciences myzheng@dicp.ac.cn Professor Zheng has been working on heterogeneous catalysis.</p> <p>Juewen Liu, PhD University of Waterloo</p>

Highlights

- Synthesis of praseodymia nanorods and nanoparticles
- Excellent multi-functional oxidase-like activities of praseodymia nanomaterials
- Colorimetric sensing of L-cysteine and fluoride using praseodymia nanorods

Graphical abstract



Multi-functional oxidase-like activity of praseodymia nanorods and nanoparticles

Lei Jiang ^{a,*}, Yaning Han ^a, Susana Fernández-García ^b, Miguel Tinoco ^{b,c}, Zhuang Li ^a, Pengli Nan ^a, Jingtao Sun ^a, Juan J. Delgado ^{b,e}, Huiyan Pan ^{b,d}, Ginesa Blanco ^{b,e}, Javier Martínez-López ^f, Ana B. Hungría ^{b,e}, Jose J. Calvino ^{b,e}, Xiaowei Chen ^{b,e,*}

^a Heavy Oil State Laboratory and Center for Bioengineering and Biotechnology, China University of Petroleum (East China), Qingdao, 266580, China

^b Departamento de Ciencia de los Materiales, Ingeniería Metalúrgica y Química Inorgánica, Facultad de Ciencias, Universidad de Cádiz, Campus Río San Pedro, Puerto Real (Cádiz), E-11510, Spain

^c Departamento de Química Inorgánica, Facultad de Ciencias Químicas, Universidad Complutense de Madrid, Av. Complutense S/N, Madrid (Madrid) E-28040, Spain

^d Henan Key Laboratory of Industrial Microbial Resources and Fermentation Technology, College of Biological and Chemical Engineering, Nanyang Institute of Technology, Nanyang, 473004, China

^e Instituto Universitario de Investigación en Microscopía Electrónica y Materiales (IMEYMAT), Universidad de Cádiz, Campus Río San Pedro, Puerto Real (Cádiz), E-11510, Spain

^f Departamento de Ciencias de la Tierra, Universidad de Cádiz, Campus Río San Pedro, Puerto Real (Cádiz), E-11510, Spain

* Corresponding authors: L. Jiang, tel: 0086-532-86981568, fax: 0086-532-86981569, Email address: leijiang@upc.edu.cn; X. Chen, tel: 0034-956-012741, Email address: xiaowei.chen@uca.es;

Abstract

The ability to mimic protein-based oxidase with multi-functional inorganic nanozymes would greatly advance biomedical and clinical practices. Praseodymia (PrO_x) nanorods (NRs) and nanoparticles (NPs) have been synthesized using hydrothermal and precipitation methods. Both PrO_x catalysts with different morphologies exhibit significantly higher oxidase-like activities (Michaelis-Menten constant $K_m \leq 0.026$ mM) than commercial PrO_x and most so-far-reported artificial enzymes. One of the substrates, dopamine, can be oxidized and further polymerized to generate polydopamine in acidic conditions. Akin to CeO_2 , which is a well-studied nanozyme, a different mechanism involving holes⁺, oxygen vacancies and oxygen mobility over PrO_x catalysts has been proposed in this work. However, fluoride ions were found to impose opposite effects on the oxidase-mimicking activity of PrO_x and CeO_2 , implying a promising path for the exploration of new nanozymes. In support of this, PrO_x was further applied in colorimetric sensing of L-cysteine and fluoride with high sensitivity.

Keywords: praseodymia, nanorods, nanoparticles, artificial enzyme, oxidase

1. Introduction

Oxidase is one of the most important multi-functional enzyme family in nature. This kind of enzymes has ability to oxidize chemicals containing groups such as amino, polyphenol or sulfur ^[1]. Mimicking or replacing protein-based oxidase would significantly advance both biomedical research and biochemical applications. As a means to an end, recent studies have shown the development of many attractive oxidase-mimicking nanozymes involving noble metals (Pt, Au and Ag) ^[2] or metal oxides (Fe₃O₄, CeO₂, CuO, MnO₂ and Mn₃O₄) ^[2]. A representative nanozyme is CeO₂, a rare earth oxide (REO) with excellent oxygen storage capability, rich surface charges, and thus, multiple oxidase-like properties ^[3]. Lately, Chen et al. reported the so-far most active oxide-mimicking Mn₂O₃ (surface area 8.5 m²/g) with kinetic parameter K_m of 0.13 mM ^[4]. Despite the tremendous efforts, the exploration of nanozymes with high catalytic activity and selectivity remains a great challenge.

Praseodymium is the neighbor of cerium in the periodic table of elements. CeO₂ is the predominant stoichiometry of cerium oxide, while the common phase of praseodymium oxide under ambient condition is roughly Pr₆O₁₁ ^[5, 6]. Pr₆O₁₁ can be considered as an oxygen-deficient modification of cubic fluorite-like PrO₂ and contains already one third of Pr in its trivalent state and two thirds of Pr⁴⁺. Pr₆O₁₁ has been reported to have the highest oxygen mobility of all undoped REOs ^[7]. From a doping point of view, it can be attributed to the fact that Pr⁴⁺ is naturally “doped” with Pr³⁺ in Pr₆O₁₁. In this sense, praseodymia has a promising potential to be a catalytic artificial enzyme because of its Pr³⁺/Pr⁴⁺ pair. It has been used as catalyst additive or support in

1 catalytic oxidation of CO, methanol, methane ^[8] and soot ^[9], decomposition reactions
2
3 of organic molecules such as 2-propanol, oxidative coupling of methane and liquid-
4
5 phase benzylation. For soot oxidation, three-dimensionally ordered macro-porous
6
7 praseodymia was significantly more active than ceria ^[9]. Our previous studies have
8
9 shown that Pr-doped ceria nanocubes are very active as artificial enzymes, from oxidant
10
11 (oxidase-like) to antioxidant (hydroxyl radical scavenging), as well as paraoxon
12
13 degradation (phosphatase-like) activities ^[3, 10]. However, application of praseodymia as
14
15 an oxidase has not been ever studied yet.
16
17
18
19
20
21

22 The preparation method can strongly affect textural, structural and redox
23
24 features of praseodymia, such as phase composition, surface area, particle morphology
25
26 or size and Pr³⁺/Pr⁴⁺ ratio on surface. These properties subsequently tune their catalytic
27
28 activities as nanozymes. Both praseodymia NRs and NPs can be synthesized via
29
30 precipitation, hydrothermal, solvothermal and microwave-assisted methods ^[11], after
31
32 thermal annealing of Pr(OH)₃ or thermal decomposition of praseodymium compounds
33
34 ^[12]. Despite Pr₆O₁₁ is one of well-known praseodymia phases, it is true that Pr³⁺/Pr⁴⁺
35
36 ratio can change easily, depending on the preparation or storage conditions of the oxide
37
38 ^[13]. For this reason, we will henceforth use the PrO_x formula to refer praseodymia.
39
40
41
42
43
44
45
46
47

48 In this work, PrO_x NRs and NPs, with relatively high surface areas, have been
49
50 synthesized using hydrothermal and precipitation methods. Their oxidase-like activities
51
52 for oxidation of 3,3',5,5'-tetramethylbenzidine (TMB), 2,2-azinobis-(3-
53
54 ethylbenzothiazoline-6-sulfonic acid (ABTS), o-phenylenediamine (OPD), and
55
56 dopamine (DOPA) have been studied using commercial praseodymia as a reference
57
58
59
60
61

1 sample. The mechanism and key intermediates, as well as the effects of anions and
2
3 amino acids have been investigated to use PrO_x as a new nanozyme and promote the
4
5 development of biomarker sensors for L-cysteine and F^- anions.
6
7

8 **2. Materials and Methods**

9 *2.1. Synthesis of PrO_x NRs and NPs*

10
11 A hydrothermal method was used to synthesize PrO_x NRs (PrO_x -NR) [11,14]. 240
12
13 mL mixture of 6 M NaOH (Alfa Aesar, 98%) and 0.05 M $\text{Pr}(\text{NO}_3)_3 \cdot 6\text{H}_2\text{O}$ (Aldrich,
14
15 99.9%) aqueous solution was stirred in a 300 mL Teflon container for 30 min. Then,
16
17 this container was sealed and placed in a stainless steel autoclave. The autoclave was
18
19 heated to 180 °C and maintained at this temperature for 24 h. Afterwards, the autoclave
20
21 was cooled down to room temperature and the resulting suspension was centrifuged
22
23 and washed with deionized water several times and then with ethanol once (Panreac,
24
25 Absolute Ethanol). Finally, sample was dried at 80 °C for 24 h in an oven and calcined
26
27 at 500 °C for 4 h in a muffle furnace.
28
29
30
31
32
33
34
35
36
37
38

39 For the synthesis of PrO_x NPs (PrO_x -NP), a precipitation method was used [15].
40
41 An aqueous solution of 0.067 M $\text{Pr}(\text{NO}_3)_3 \cdot 6\text{H}_2\text{O}$ (Alfa Aesar, 99.9%) was mixed with
42
43 4.9 M $\text{NH}_3 \cdot \text{H}_2\text{O}$ in 75 mL solution and stirred at 80 °C for 3 h. The mixture was kept
44
45 at room temperature for 48 h followed by centrifugation for 30 min. The obtained
46
47 precipitate was rinsed with ultrapure water and ethanol over three times, dried at 100
48
49 °C in an oven for 10 h, and finally calcined at 500 °C for 3 h in a muffle furnace.
50
51
52
53
54
55

56 A commercial Pr_6O_{11} (99.99%) sample (PrO_x -C) was purchased from Alfa
57
58 Aesar.
59
60
61
62
63
64
65

2.2. Physical and compositional characterization

X-Ray diffraction (XRD) patterns were recorded on a D8 ADVANCE diffractometer of Bruker using a Cu K α radiation, with a range of 25-75 $^\circ$, a step of 0.02 $^\circ$ and a step time of 1 s. Phase identification and composition calculation were performed using TOPAS v5 software from Bruker. Brunauer-Emmett-Teller (BET) surface areas of samples were determined in a Micromeritics TriStar - 3020 via N $_2$ adsorption at -196.15 $^\circ$ C. Prior to analysis, samples were degasified at 150 $^\circ$ C for 8 h under vacuum.

The surface chemical composition and oxidation states of samples were characterized by X-ray photoelectron spectroscopy (XPS). Analyses were performed on an ESCALAB 250Xi instrument. Spectra were recorded using monochromatized Al K α X-Ray (1486.6 eV), with an X-ray power of 150 W. The spectrometer was operated in a constant analyzer energy mode, with pass energy of 30 eV. Powder samples were pressed into a disk, which was stuck on a double-sided adhesive conducting polymer tape and analyzed without further treatment. The binding energy scale was calibrated with respect to the C *1s* signal at 284.8 eV. CasaXPS software, version 2.3.23.PR1.0 (Casa Software Ltd., Devon, UK), was used for spectra processing.

The morphology and size of PrO $_x$ samples were studied by Scanning Electron Microscopy (SEM). A FEI Nova Nano SEM450 microscope was used at 3 to 10 kV accelerating voltages with a working distance of 5 mm. PrO $_x$ samples were also characterized by High Resolution Transmission Electron Microscopy (HRTEM) and Scanning Transmission Electron Microscopy-High Angle Annular Dark Field imaging

1 (STEM-HAADF) using JEOL 2010-F and FEI Titan³ Themis 60–300 aberration-
2
3 corrected microscopes. HRTEM images were obtained with 0.19 nm spatial resolution
4
5 at Scherzer defocus and STEM-HAADF images were acquired by using an electron
6
7 probe of 0.5 nm of diameter at a camera length of 8 cm.
8
9

10
11
12 Temperature Programmed Reduction with H₂ (H₂-TPR) started with a
13
14 pretreatment consisting in an oxidation under a 5% O₂/He flow (60 mL/min) at 500 °C
15
16 for 1 h. After the oxidation pretreatment, samples were cooled in the same 5% O₂/He
17
18 flow down to 150 °C, and then, the flow was switched to pure He cooling down to room
19
20 temperature. The samples were reduced in a 60 mL/min flow of 5% H₂/Ar with a
21
22 heating rate of 10 °C/min up to a maximum reduction temperature of 950 °C, keeping
23
24 them at this final temperature for 1 h. The outlet of H₂-TPR equipment was connected
25
26 to a Thermostar GSD301T1 or a PrismaPlusTM mass spectrometer of Pfeiffer Vacuum.
27
28
29 The evolution of the mass/charge ratio (m/z) = 18 was used to monitor the formation of
30
31 H₂O during the H₂-TPR process.
32
33
34
35
36
37
38
39
40

41 UV-Vis specular and diffuse reflectance measurements were carried out using an
42
43 SHIMADZU 2600i UV–Vis-NIR double-beam spectrophotometer. The spectra in 220 -
44
45 1400 nm range were registered in an integrating sphere. Diffuse reflectance spectra were
46
47 transformed into apparent absorption spectra using the Kubelka–Munk function ($F(R)$). The
48
49 direct and indirect optical band gap of materials was determined through construction of
50
51 Tauc plots by plotting $(F(R)hv)^n$ against (hv) , with $n=2$ or $n=1/2$, for direct and indirect
52
53 transitions, respectively. The optical band gap was obtained by extrapolating the linear part
54
55 of this plot to the energy axis.
56
57
58
59
60
61
62
63
64
65

1 Fourier transform infrared (FTIR) spectra of the samples were obtained on a
2
3 Nicolet 6700 instrument. Samples suspended or diluted in water were added dropwise
4
5 to a compressed potassium bromide IR-transparent pellet, and then dried to remove all
6
7 water. FTIR spectra were registered in the range of 4000-500 cm^{-1} .
8
9

10
11
12 Electron Paramagnetic Resonance (EPR) spectra were measured in a dark room on a
13
14 Bruker ELEXSYS E500 spectroscope. Samples were prepared by dispersing 3 mg/mL
15
16 PrO_x in pH 4 acetate buffer. 5,5-dimethyl-1-pyrroline-N-oxide (DMPO) was used as the spin
17
18 trap for oxygen vacancies while 2,2,6,6-Tetramethylpiperidinoxy (TEMPO) was used for
19
20 photo-induced electron, which in turn indicates the generation of hole⁺. A light source from
21
22 a 300 W xenon lamp (PLS-SXE300, BOFEILAI) was used to generate light at the
23
24 wavelength range of 320 – 780 nm.
25
26
27
28
29
30

31
32 The generation of $\text{HO}\cdot$ over $\text{PrO}_x\text{-C}$ sample was monitored by using a
33
34 fluorescent probe terephthalic acid (TA) which can react with the radicals to form a
35
36 highly fluorescent product, 2-hydroxy TA (TAOH). H_2O_2 was added to generate $\text{HO}\cdot$
37
38 radicals as negative (without $\text{PrO}_x\text{-C}$) and positive control (with $\text{PrO}_x\text{-C}$). The
39
40 fluorescence at 435 nm of TAOH was measured with excitation at 315 nm via a
41
42 fluorescent spectrometer (FluoroMax-4, Horiba Jobin Yvon, France).
43
44
45
46
47
48

49 *2.3. Artificial enzyme activities*

50
51
52

53 The oxidase mimetic activities for the oxidation of colorless TMB, ABTS,
54
55 DOPA and OPD were studied over three kinds of PrO_x catalysts. The oxidized TMB,
56
57 ABTS, DOPA and OPD have characteristic UV-vis absorbance peaks at 652, 405, 450
58
59
60
61
62
63
64
65

1 and 450 nm, respectively. All these organic chemicals were bought from Sigma
2 Aldrich. The PrO_x suspension was prepared dispersing powder samples in Milli Q water
3 after washing and centrifuging at 12000 rpm for 10 min three times. All suspensions
4 were sonicated in a 100 W water bath sonicator (Kunshan, KQ-100) for 2 h before each
5 measurement. An extra-strong 500 W ultrasonic processor (VC505, Sonics & Materials,
6 Inc.) was also employed to examine the possible effect of aggregation. Radical
7 scavengers, including TEMPO and p-benzoquinone, isopropanol (hydroxyl HO•
8 scavenger) and sodium oxalate (hole⁺ scavenger), were purchased from Sigma Aldrich.
9
10
11
12
13
14
15
16
17
18
19
20
21
22

23 A 4.16 mM TMB stock solution was prepared in dimethyl sulfoxide. Then, a
24 0.2 mM TMB solution was prepared by diluting the concentrated stock solution with
25 10 mM pH 4.0 of acetate buffer. Similarly, 0.088 mM ABTS, 0.31 mM DOPA and 4
26 mM OPD solutions were prepared in 10 mM acetate buffer pH 4.0. The UV-Vis
27 absorption spectra of substrates before and after praseodymia addition were recorded
28 in a SHIMADZU UV-2450 spectrophotometer. To explore and compare the kinetic
29 activities of different samples, praseodymia amount was kept constant at 20 µg/mL
30 with TMB at 0.05, 0.1, 0.15, 0.2, 0.25, 0.3, 0.35 mM to calculate Michaelis-Menten
31 parameter K_m and maximum reaction rate V_{max} .
32
33
34
35
36
37
38
39
40
41
42
43
44
45
46
47
48

49 Inhibition effect of L-cysteine was measured in solution of TMB and 45 µg/mL
50 PrO_x-NR. Concentration of L-cysteine was varied from 0 to 10 µM. Effects of other
51 amino acids, including 4 µM lysine (Lys), phenylalanine (Phe), arginine (Arg),
52 histidine (His), tyrosine (Tyr), Homocysteine (Hcy), glutathione (GSH) and glycine
53 (Gly), were compared with 4 µM L-cysteine at the same conditions.
54
55
56
57
58
59
60
61
62
63
64
65

2.4. Fluoride effect and detection

To compare impacts of several anions, including F⁻, on the oxidase activity of PrO_x-NR, 90 μM TMB and 90 μg/mL PrO_x-NR suspension, were added to 5 mM NaF, Na₂SO₄, NaCl, Na₃PO₄, NH₄Br and Na₂CO₃ solutions. Absorbance changes @ 652 nm were measured. For example, the quantitative detection of fluoride in commercial toothpaste (Oral B from supermarket) was measured as follows. Briefly, 1 g toothpaste was vigorously mixed with 32 mL water and filtered through a Millipore Amicon Ultra-15 (3 kDa molecular weight cutoff) ultrafiltration membrane. The filtrate was centrifuged at 15000 rpm for 10 min and the supernatant was collected after centrifugation. Standard addition method^[16] was used to analyze fluoride concentration while minimizing the matrix effect. NaF of 0, 10.7, 21.4, 32.2, 42.9, 53.9, and 64.3 μM concentrations were added to 1 mL solution of 90 μg/mL PrO_x-NR in pH 4.0 10 mM acetate buffer to form spiked samples. Then 30 μL of collected supernatant was added to the mixture and stirred for 10 min. Finally, 90 μM TMB was added and absorbance at 652 nm was measured.

3. Results and discussion

Two types of PrO_x samples, *i.e.* PrO_x-NR and PrO_x-NP were synthesized and characterized, together with a commercial PrO_x-C sample. All of them are dark powders (Fig. 1a), but both PrO_x-NR and PrO_x-NP samples are more brown-colored than PrO_x-C. Their XRD patterns (Fig. 1b) show that all the diffraction peaks can be attributed to a fluorite-like structure, face-centered cubic lattice Pr₆O₁₁ (Fm-3m, JCPDS 42-1121).

1 The diffraction peaks of commercial $\text{PrO}_x\text{-C}$ are much narrower than those of $\text{PrO}_x\text{-NR}$
2
3 and $\text{PrO}_x\text{-NP}$, indicating that the crystallinity of $\text{PrO}_x\text{-C}$ is much better than those of the
4
5 synthesized PrO_x samples. Using diffraction peak at 28° , the average particle sizes of
6
7 $\text{PrO}_x\text{-NR}$, $\text{PrO}_x\text{-NP}$ and $\text{PrO}_x\text{-C}$ were calculated by Scherrer equation to be 7.1, 10.3
8
9 and 49.8 nm, respectively.
10
11
12

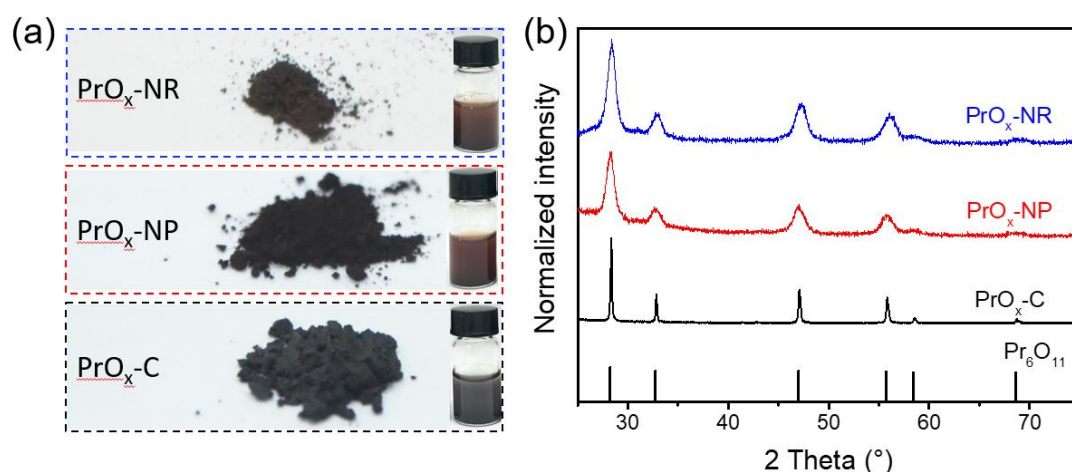


Fig. 1. (a) Photographs of three types of PrO_x samples in solid state and suspension in water, including the $\text{PrO}_x\text{-NR}$ synthesized by hydrothermal method, $\text{PrO}_x\text{-NP}$ synthesized by precipitation and commercial $\text{PrO}_x\text{-C}$. (b) XRD patterns of three PrO_x samples.

Fig. 2 shows SEM images of the three PrO_x samples at low and high magnifications. These samples show different morphologies. $\text{PrO}_x\text{-NR}$ sample prepared by the hydrothermal route presents uniform NR shape. The PrO_x NRs, with diameters in the 20 to 65 nm range and length up to 10 μm , are entangled (Figs. 2a and 2b). $\text{PrO}_x\text{-NP}$ synthesized by precipitation features irregular morphology particles or agglomerates with size less than 5 μm (Fig. 2e). High resolution SEM image (Fig. 2f) of this sample indicates its surfaces of uneven roughness. Commercial $\text{PrO}_x\text{-C}$ also appears to be constituted by agglomeration of large irregularly-shaped particles. $\text{PrO}_x\text{-C}$ particles (Figs. 2i-2j) are not only larger but also show much smoother surfaces than

1 those of PrO_x-NP.
2

3 TEM and STEM-HAADF images of the three PrO_x samples are also illustrated
4 in Fig. 2. Low magnification TEM image of PrO_x-NR (Fig. 2c) and STEM images of
5 PrO_x-NP (Fig. 2g) and PrO_x-C (Fig. 2k) samples confirm the size and morphology
6 results observed by SEM. The crystalline nature of all the samples is clearly appreciated
7 in HRTEM and STEM-HAADF images at the bottom row of Fig. 2. Digital diffraction
8 pattern (DDP) analysis of the selected area of HRTEM image of PrO_x-NR (inset in Fig.
9 2d) shows the major reflections of the fluorite type structure, which is characteristic of
10 higher praseodymium oxide (eg. PrO₂). Similar to PrO_x-NR catalyst, DDP analysis of
11 selected areas of PrO_x-NP (Fig. 2h) and PrO_x-C (Fig. 2l) catalysts clearly confirm their
12 fluorite type phase. Interestingly, the DDP of PrO_x-C shows the presence of additional
13 spots that it is a clear indication of a superstructure formed by the ordering of oxygen
14 vacancies. A more detailed explanation is included in the supporting information (Fig.
15 S1a). In addition, the PrO_x-NP sample is comprised of small crystals in nanometer scale
16 as shown in Figs S1b, which is in good agreement with average particle size of 10.3 nm
17 of PrO_x-NP calculated using Scherrer equation.
18
19
20
21
22
23
24
25
26
27
28
29
30
31
32
33
34
35
36
37
38
39
40
41
42
43
44
45
46
47
48
49
50
51
52
53
54
55
56
57
58
59
60
61
62
63
64
65

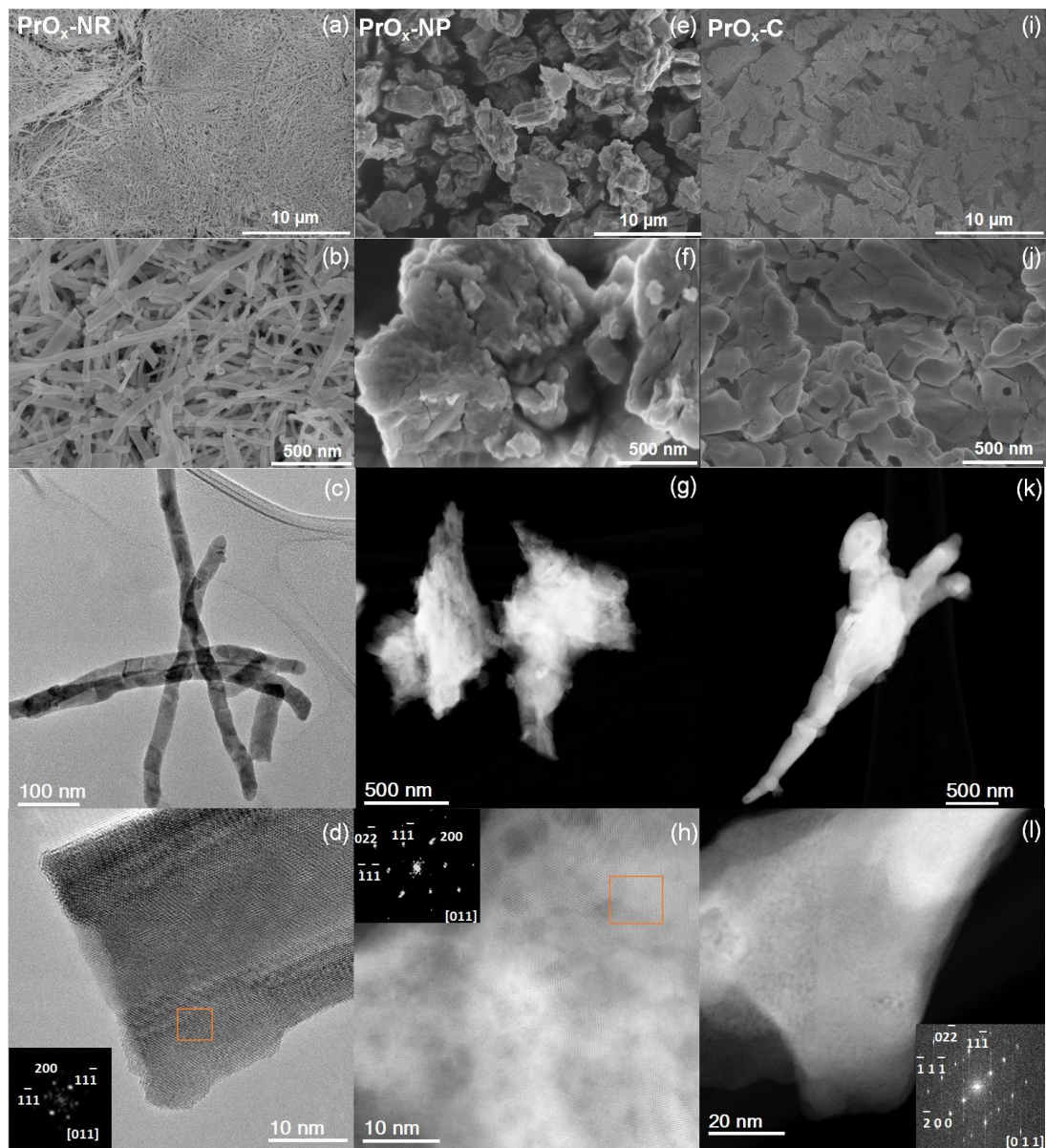


Fig. 2. SEM, TEM and STEM-HAADF images of (a-d) PrO_x-NR, (e-h) PrO_x-NP and (i-l) PrO_x-C samples

BET specific surface areas and total pore volumes of three samples were measured by N₂ physisorption (Table 1). PrO_x-NP possesses the highest surface area, 65 m²/g, followed by PrO_x-NR with 27 m²/g and, finally, PrO_x-C with just 4 m²/g, a value characteristic of typical bulk materials. The total pore volume data of these samples follow the same trend. These results are in good agreement with the above-mentioned XRD and TEM results. Poor crystallinity and small size of PrO_x-NR and

1 PrO_x-NP lead to their high BET specific surface areas, while PrO_x-C presents bigger
2
3 particle size, much better crystallinity and much lower surface area.
4
5

6 XPS spectra of three PrO_x samples are shown in Fig. 3 for Pr *3d*, O *1s* and C
7
8 *1s* core levels. For Pr *3d* core level (Fig. 3a), peak deconvolution was performed by
9 following the analysis reported by Sinev et al. ^[17]. All spectra could be fitted using 7
10 peaks, i.e. peaks labelled as *a*, *b* and *c* are for 3d_{5/2} component, and *a'*, *b'* and *c'* peaks
11 are their corresponding 3d_{3/2} counterparts. An extra peak, existing only in the 3d_{3/2}
12 component, and labelled as *t'*, was also included as reported previously ^[17]. There is no
13 agreement yet on the assignment of peaks to Pr³⁺ or Pr⁴⁺ oxidation states unequivocally
14 in the literature ^[17-19]. However, Borchert et al. ^[18] proposed a method to determine the
15 oxidation degree of Pr by using peaks *a-a'*, which are undoubtedly related with Pr⁴⁺,
16 and *b-b'*, which appear for both oxidation states. Although they warned that the
17 calculation could lead to a rough approximation, this is one of the most consistent
18 attempts to determine Pr oxidation state using XPS. Here we use this method to
19 calculate Pr³⁺ percentage and results in Table 1 indicate the mixed valence nature of
20 three PrO_x samples with all surface Pr³⁺ percentage at 60 – 70%.
21
22
23
24
25
26
27
28
29
30
31
32
33
34
35
36
37
38
39
40
41
42
43
44
45
46
47
48
49
50
51
52
53
54
55
56
57
58
59
60
61
62
63
64
65

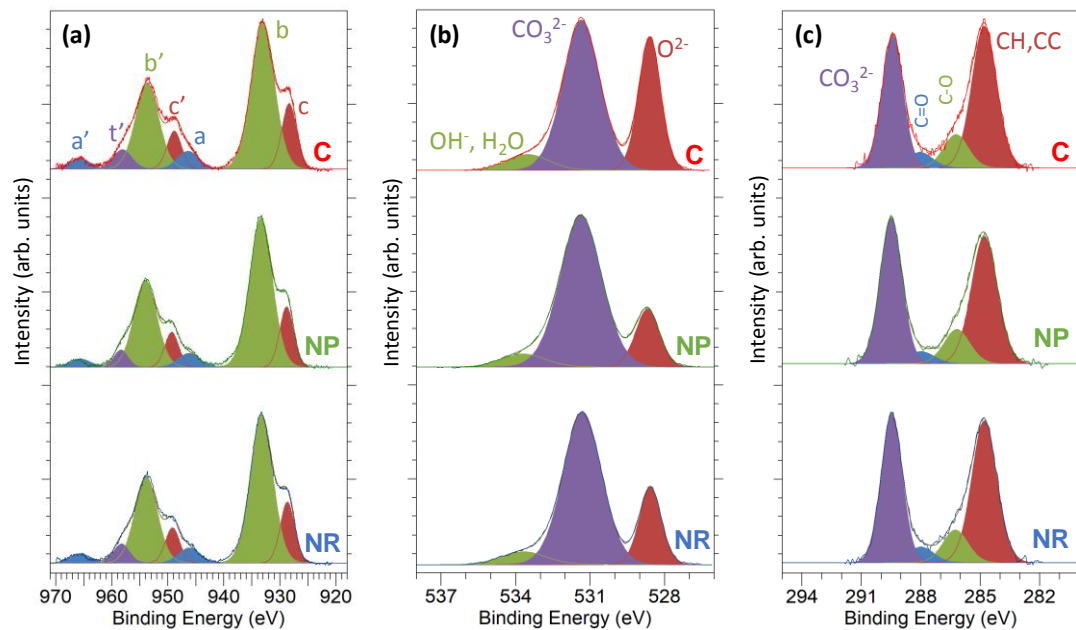


Fig. 3. XPS spectra of (a) Pr 3d, (b) O 1s and (c) C 1s of PrO_x-NR (blue), PrO_x-NP (green) and PrO_x-C (red) samples.

Table 1 Physicochemical properties and catalytic activities of PrO_x samples

Catalyst	BET surface area ^a (m ² g ⁻¹)	Total pore volume ^a (cm ³ g ⁻¹)	Percentage of Pr ³⁺ ^b (%)	Ratio of O _{carbonate} /O _{lattice} ^b	Indirect band gap ^c (eV)	Direct band gap ^c (eV)	K _m ^d (mM)
PrO _x -NR	27	0.062	66	3.4	1.10	2.06	0.026
PrO _x -NP	65	0.530	68	4.5	0.79	2.12	0.018
PrO _x -C	4	0.021	61	1.9	0.77	2.20	0.180

^a Obtained from N₂ physisorption

^b Calculated using XPS data

^c Determined using Tauc method

^d Kinetic parameters using TMB as substrate

Further insight about the chemical composition of samples is given by analyzing O 1s and C 1s core levels (Fig. 3b and 3c). It is well known that praseodymia reacts readily with atmospheric water and CO₂ when it is exposed to air [20, 21]. Analysis of O 1s and C 1s core levels confirms these phenomena. O 1s spectra in Fig. 3b can be fitted using a combination of 3 peaks: one peak around 528.6 eV that could be attributed to lattice oxygen (O²⁻); a second feature, the most intense in all the samples, around

1 531.3-531.4 eV that can be assigned to carbonates (CO_3^{2-}); and a third weak peak at
2
3 533.5-533.7 eV, due to the presence of OH^- or water groups. Relative intensity of
4
5
6 oxygen from carbonate and lattice after fitting is presented in Table 1. It shows that
7
8
9 there could be a correlation between surface area and $\text{O}_{\text{carbonate}}/\text{O}_{\text{lattice}}$, i.e. the higher the
10
11
12 surface area, the larger the carbonation extent.

13
14 C 1s core level in Fig. 3c also confirms the existence of carbonate on all
15
16 samples. Peaks at 284.8 eV, 286.2 eV and 288.0 eV correspond to C-C, C-O and C=O,
17
18
19 respectively, from adventitious carbon. The dominant peak at 289.4-289.5 eV is due to
20
21
22 carbonate. The presence of these carbonated species is strongly related to the high Pr^{3+}
23
24
25 content of these samples as determined by XPS. In short, the higher the surface area of
26
27
28 the PrO_x samples, the higher the carbonate content, and thus the higher the reduction
29
30
31 degree of praseodymium.

32
33 Fig. 4 shows UV-visible diffuse reflectance spectra of PrO_x catalysts.
34
35
36 Absorbance spectra of $\text{PrO}_x\text{-NP}$ and $\text{PrO}_x\text{-C}$ samples are very similar in 220-1400 nm
37
38
39 wavelength range. In comparison, $\text{PrO}_x\text{-NR}$ exhibits a quite strong absorbance in the
40
41
42 visible range between 220 to 640 nm, in agreement with previous reports [12]. This is
43
44
45 probably why $\text{PrO}_x\text{-NR}$ appears more brown-colored than the other two samples (Fig.
46
47
48 1a). As shown in XRD results, the main phase of three PrO_x catalysts is Pr_6O_{11} , which
49
50
51 contains both Pr^{3+} and Pr^{4+} oxidation states. The contribution of Pr^{3+} and Pr^{4+}
52
53
54 absorbance in UV-visible range is still in debate. Kang et al. reported that the presence
55
56
57 of oxidation state of Pr^{4+} may be the origin of the strong/broad absorption in the visible
58
59
60 region by charge transfer ($\text{O}^{2-} \rightarrow \text{Pr}^{4+}$) absorption [12]. On the other hand, previous
61
62
63
64
65

1 studies also reported Pr^{4+} does not absorb in the UV-vis region [22]. In other words, the
2
3 absorbance in the 430 – 610 nm range can be mainly attributed to Pr^{3+} . Meanwhile, Pr^{3+}
4
5 absorption bands between 430 – 490 nm due to the $^3\text{H}_4$ ground state to $^3\text{P}_1$ transition
6
7 and that the 560 – 610 nm band originated from a $^3\text{H}_4$ to $^1\text{D}_2$ transition [22]. It should be
8
9 highlighted that there is no big difference between Pr^{3+} percentages (Table 1) of PrO_x -
10
11 NR and PrO_x -NP catalysts calculated using XPS results, and Pr^{3+} percentage of PrO_x -
12
13 C is slightly lower than PrO_x with NR and NP morphologies. The reason of UV-visible
14
15 strong absorption of PrO_x -NR different with PrO_x -NP and PrO_x -C is not clear, which
16
17
18
19
20
21
22
23
24
25
26
27
28
29
30
31
32
33
34
35
36
37
38
39
40
41
42
43
44
45
46
47
48
49
50
51
52
53
54
55
56
57
58
59
60
61
62
63
64
65

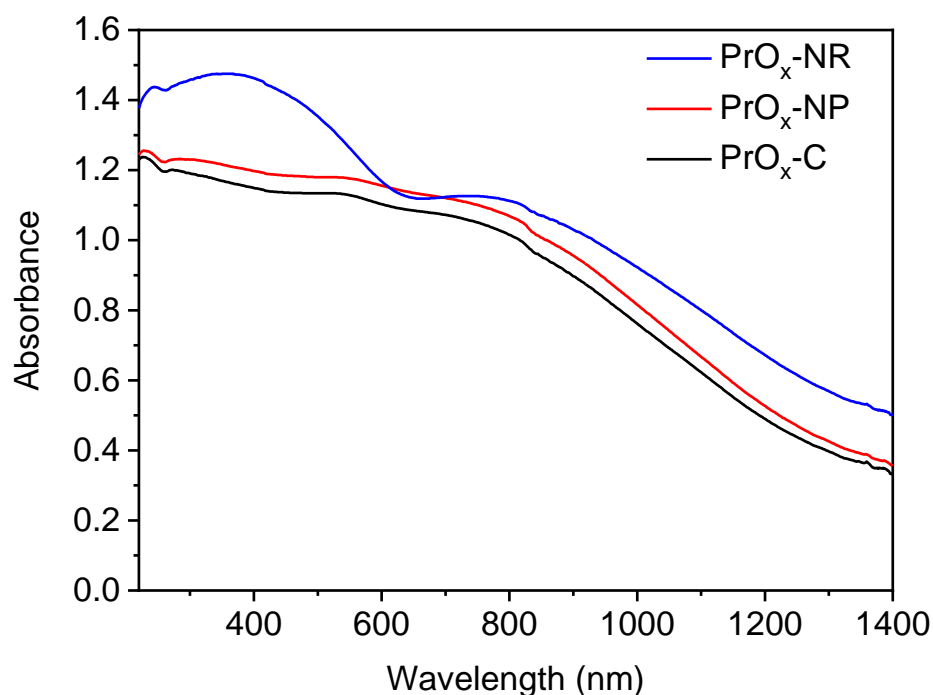


Fig. 4. UV-Visible diffuse reflectance spectra of PrO_x samples.

Using the UV-Vis diffuse reflectance results, indirect and direct band gap energies of PrO_x samples can be determined via the Kubelka-Munk function. As shown in Table 1, there is no significant difference in direct band gap values (2.06 – 2.20 eV)

1 for three PrO_x samples, in accordance with previous results in the literature [10, 23].

2
3 However, some researchers have reported higher values for direct band gap of PrO_x ,
4
5
6 from 3.15 to 4.45 eV [24]. The origin of such difference in optical properties and band
7
8
9 gap energies could stem from the synthesis methods of PrO_x . The band gap reduction
10
11
12 may be attributed to both the uplift of valence band (due to surface disorder) and
13
14
15 lowering of conducting band (due to oxygen vacancies and more defect centers) [25].
16

17 Fig. 5 displays the formation of H_2O over all PrO_x samples during H_2 -TPR
18
19 process. The redox behavior of PrO_x -NR is better than those of the other two samples.
20
21
22 Its dominant reduction peak appears at 480 °C, at lower temperature than in PrO_x -NP
23
24 (502 °C) and PrO_x -C (509 °C). The reason might be due to its smaller average
25
26
27 crystalline size (7.1 nm) than those of other two samples (10.3 and 49.8 nm) according
28
29
30 to calculation using Scherrer equation. The main reduction peak corresponds to the
31
32
33 reduction of Pr^{4+} in bulk of PrO_x samples. TPR profiles of PrO_x -NP and PrO_x -C
34
35
36 catalysts are similar in that both have a minor reduction peak at 310 or 332 °C, which
37
38
39 can be assigned to the reduction of surface Pr^{4+} and the active surface oxygen species
40
41
42 react with hydrogen to form H_2O [12, 26]. The reduction peak of PrO_x -NR at low
43
44
45 temperature is merged into an asymmetric peak at 480 °C. This result is in good
46
47
48 accordance with previous TPR data of PrO_x -NR and bulk PrO_x in the literature [26]. The
49
50
51 final product of H_2 -TPR of three PrO_x samples is expected to be Pr_2O_3 , according to
52
53
54 literature [8, 21].
55
56
57
58
59
60
61
62
63
64
65

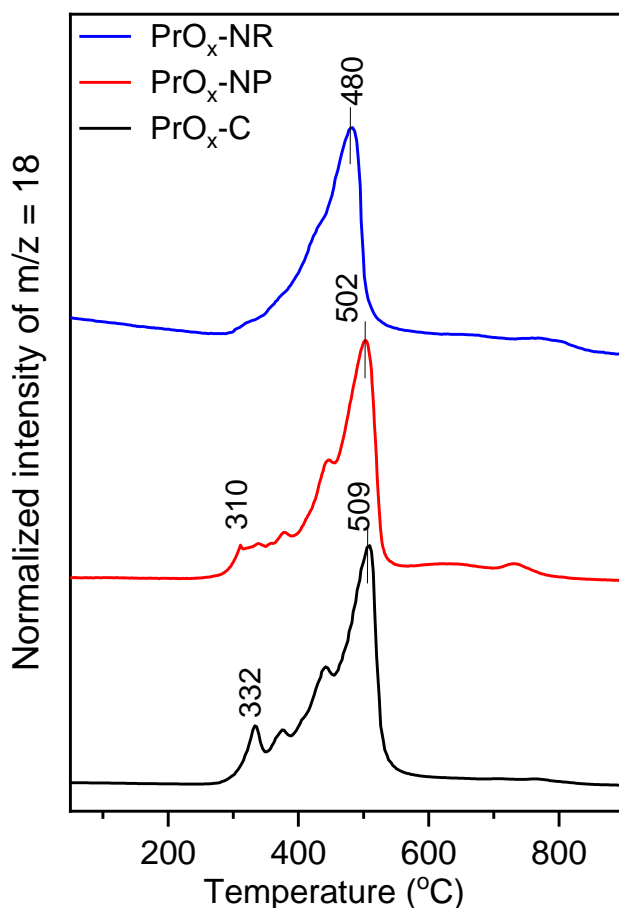


Fig. 5. H_2O evolution ($m/z=18$) during H_2 -TPR of PrO_x -NR, PrO_x -NP and PrO_x -C catalysts.

The multi-functional oxidase-like activity of PrO_x was studied by their effects in oxidizing conventional substrates including TMB, ABTS, OPD and DOPA. TMB, ABTS and OPD are chromogenic substrates with oxidable amino groups, while DOPA represents substrates with polyphenol groups. Once PrO_x samples were added to substrates in pH 4.0 acetate buffers, individual characteristic colors quickly appeared (Fig. 6a), suggesting the occurrence of oxidation of substrates. The corresponding UV-vis absorbance spectra changes of all substrates are illustrated in Fig. S2. Similar to other previously reported oxidase-like nanomaterials, the catalytic activities of PrO_x catalysts are pH-dependent and pH 4.0 is the optimum condition for all substrates (Fig.

1 6b). In comparison, TMB and DOPA are more sensitive to pH changes than ABTS,
2
3 probably because they are positively charged while ABTS is negatively charged,
4
5 inducing different adsorption and catalytic behaviors of nanozymes as previously
6
7 reported [27].
8
9

10
11 Kinetics of three PrO_x samples (Fig. S3) can be calculated by the Michaelis-
12
13 Menten equation as shown in Method in Supporting information using TMB as a
14
15 substrate and their kinetic parameters K_m are listed in Table 1. Lower K_m value means
16
17 higher oxidase activity of nanozymes. These results indicate that the oxidase-like
18
19 activities follow the order of PrO_x-NP > PrO_x-NR > PrO_x-C, exactly the same order of
20
21 their BET surface areas. More importantly, K_m values of both PrO_x-NR (0.026 mM) and
22
23 PrO_x-NP (0.018 mM) are an order of magnitude lower than that of PrO_x-C (0.18 mM),
24
25 and significantly lower than most of the reported oxidase-like nanozymes. Their
26
27 maximum reaction rates V_{max} also show same tendency, 0.031, 0.029 and 0.0013
28
29 mM/min, respectively. Table S1 compares K_m and V_{max} values from this study with
30
31 those of the so-far-reported nanozymes in TMB oxidation since 2007, including high
32
33 activity of Mn₂O₃ nanoparticles [4]. The comparison suggests that PrO_x-NP and PrO_x-
34
35 NR exhibit relatively higher activities than those nanozymes of similar levels of V_{max}
36
37 (Table S1).
38
39
40
41
42
43
44
45
46
47
48
49

50 Fig. 6c compares steady-state catalytic activities of three PrO_x catalysts, as
51
52 well as those of three compounds of praseodymium, Pr₂O₃, Pr₂(CO₃)₃, and Pr(OH)₃.
53
54 There is almost no oxidase activity of TMB oxidation over these three Pr-containing
55
56 compounds with solely Pr oxidation state of +3. At the beginning of reaction (< 1 min),
57
58
59
60
61
62
63
64
65

1 PrO_x-NP performs faster than PrO_x-NR, but over longer time (> 2 min), PrO_x-NR is
2
3 better than PrO_x-NP. This is probably because the aggregated state of PrO_x-NP partly
4
5 inhibits the following attachment of substrates, which was further examined with the
6
7 help of extra-strong ultrasonicator in Fig. S4. However, PrO_x-NR is much better
8
9 dispersed in solution; therefore, it exhibits better long-term catalytic activity.
10
11 Furthermore, similar K_m and V_{max} values of PrO_x-NR and PrO_x-NP means that TMB
12
13 oxidation occurs with similar kinetic rate, i.e. similar amount of TMB is oxidized over
14
15 both samples. Often the catalytic activities of nanomaterials can be compared as activity
16
17 per unit surface area [28]. In this study, TMB oxidation takes place on the surface of PrO_x
18
19 samples, considering that the BET surface area of PrO_x-NR is less than half of PrO_x-
20
21 NP, it means that the activity per unit area on PrO_x-NR surface is higher than that of
22
23 PrO_x-NP.
24
25
26
27
28
29
30
31

32
33 As mentioned before, the Pr³⁺/Pr⁴⁺ ratio of PrO_x can change easily with storage
34
35 conditions so that it bears a risk of phase change upon exposure to air after long time
36
37 storage [21]. Fig. S5a shows XRD patterns of three PrO_x catalysts stored in air for years.
38
39 Pr(OH)₃ phase can be observed on all PrO_x samples. However, PrO_x-NR stored for 9
40
41 years and PrO_x-NP stored for 3 years contain less Pr(OH)₃ phase and more PrO₂ and
42
43 Pr₆O₁₁ phases than PrO_x-C stored for 5 years. Since calcination of Pr(OH)₃ is a step of
44
45 synthesis of PrO_x, it is reasonable to recalcine PrO_x samples exposed in air for a long
46
47 time at 500 °C to obtain pure PrO_x phase again. This hypothesis is confirmed, which
48
49 calcination at 500 °C leads to the formation of pure Pr₆O₁₁ phase again as shown in Fig.
50
51
52
53
54
55
56
57
58
59
60
61
62
63
64
65

year storage. Both samples were recalcined at 500 °C for 4 h to regenerate Pr₆O₁₁ and effective TMB oxidation is observed, suggesting the good stability of PrO_x samples.

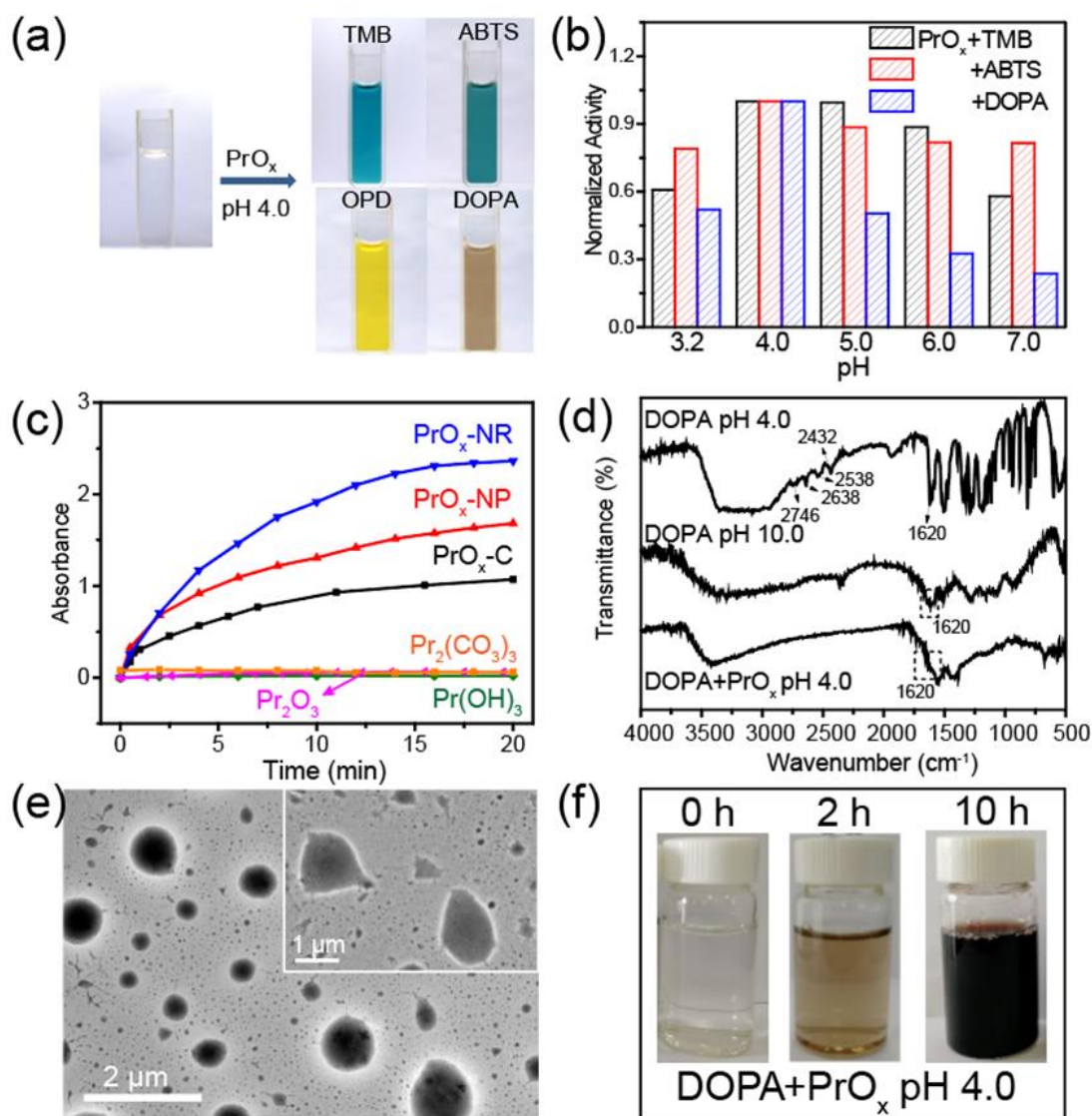


Fig. 6. (a) Colorless TMB, ABTS, OPD and DOPA substrates can be catalytically oxidized by PrO_x to generate characteristic colors at pH 4.0. (b) pH-dependence of oxidase-like activities of PrO_x-NR samples. Normalized activity of each reaction was obtained by normalizing absorbance of oxidized TMB at 652 nm, oxidized ABTS at 405 nm and oxidized DOPA at 450 nm by absorbance of un-oxidized substrates, respectively. (c) Absorbance changes at 652 nm of 0.2 mM TMB in pH 4.0 acetate buffer when 92 μg/mL catalysts (PrO_x, Pr₂O₃, Pr₂(CO₃)₃, and Pr(OH)₃) were added. (d) FTIR spectra of 1 M DOPA at conditions of pH 4.0, pH 10.0 and pH 4.0 with 1.1 mg/mL PrO_x-NR. (e) Optical microscopic image of DOPA solution after addition of PrO_x-NR in pH 4.0 solution, forming dark polydopamine spheres. Inset is the image of DOPA solution without PrO_x-NR. (f) Photographs of PrO_x-NR oxidizing and polymerizing dopamine in acidic condition.

1 Since PrO_x-NR nanozyme presents the highest steady-state activity and similar
2
3 *K_m* value to PrO_x-NP, further studies to understand mechanism and influences of amino
4
5 acids and anions focus on this catalyst. The activities of PrO_x-NR catalysts are so high
6
7 that they can even enable the polymerization of concentrated DOPA to polydopamine
8
9 (PDA) in acidic solution. FTIR spectra of DOPA at pH 4.0 and 10.0 and pH 4.0 with
10
11 PrO_x-NR conditions are compared in Fig. 6d. The characteristic bands at 2746, 2638,
12
13 2538 and 2432 cm⁻¹ of DOPA disappear at pH of 10.0 and at pH of 4.0 with PrO_x-NR,
14
15 because the polymerization of DOPA changes NH₂ to secondary amine [29]. Meanwhile,
16
17 the width of 1620 cm⁻¹ peak increases after polymerization at pH of 10.0 and at pH of
18
19 4.0 with addition of PrO_x-NR, probably due to C=C stretching vibration of indole
20
21 structure formed by intramolecular cyclization reactions [30]. Further, results in Fig. 6e
22
23 and 6f also demonstrate the gradual oxidation and induced-polymerization of DOPA.
24
25
26
27
28
29
30
31
32

33
34 It is well known that DOPA can be oxidized and self-polymerized to PDA in
35
36 basic (pH >8) media, but not in neutral and acidic media [31-34]. PDA is a wet bio-
37
38 adhesive that has unique photo-physical properties for a wide range of biomedical
39
40 applications. To oxidize and polymerize PDA in acidic condition usually involves
41
42 unconventional tools such as UV-illumination [31, 32], plasma treatment [33], high
43
44 temperature (over 120 °C for 16 h) [34]. To the best of our knowledge, this is the first
45
46 time that oxidative self-polymerization of PDA is achieved in an acidic environment
47
48 with solely the help of inorganic nanoparticles as catalysts. It is worth noting that an
49
50 employment of PrO_x-NR as oxidase to synthesize PDA may also be beneficial to widen
51
52 the pH range of application of PDA.
53
54
55
56
57
58
59
60
61
62
63
64
65

1 The key reasons for such high catalytic performance of PrO_x may be attributed
2
3 to the important intermediate holes⁺, which is remarkably different from other
4
5 nanozymes. So far most reported oxidase-like nanozymes, such as CeO₂, MnO₂, iron-
6
7 based materials etc. [2], interact with molecular oxygen (or other oxidizing reagents) to
8
9 generate intermediate superoxide radical anion (O₂^{•-}) as the key oxidants in the
10
11 oxidation process. In order to elucidate the mechanism of oxidase-like property of PrO_x-
12
13 NR, several scavengers corresponding to different reactive oxygen species and charge
14
15 carriers were applied to PrO_x-TMB system. For example, p-benzoquinone [35] in Fig. 7a
16
17 and TEMPO [36] in Fig. 7b were used to capture O₂^{•-}, while isopropanol [37] is a hydroxyl
18
19 (HO[•]) scavenger and sodium oxalate [38] was added to eliminate hole⁺ [39]. Results show
20
21 that only sodium oxalate (hole⁺ inhibitor) can significantly affect the oxidase-like
22
23 activity and the inhibition level is highly dependent on the amount of eliminator. On
24
25 the contrary, the other three inhibitors show no influence within the concentration range
26
27 studied in this work. These results imply that, in PrO_x-catalyzed oxidation, the key
28
29 intermediate is hole⁺, not the conventional radicals like O₂^{•-} or HO[•]. To the best of our
30
31 knowledge, this is the first time that hole⁺ was reported for the activity of nanozyme.
32
33 This feature of PrO_x is also in clear contrast to its affiliated oxide CeO₂, which is well
34
35 known for generating O₂^{•-}. Such hole⁺-induced oxidation is also dependent on pH
36
37 values (Fig. 6b), probably because that the surface hydroxyls can react with hole⁺ to
38
39 form hydroxyl radicals and thus the total oxidative capacity decreases at higher pH
40
41 conditions.
42
43
44
45
46
47
48
49
50
51
52
53
54
55
56

57
58 The generation of holes⁺ was further tested by EPR spectra. It was known that
59
60

1 photoexcitation may lead to the concomitant generation of electron/hole⁺ pairs [40]. The
2
3 identification of photoinduced electrons by EPR is a clear indication of the presence of
4
5 hole⁺. The spin label TEMPO does not react with oxidative intermediates such as O₂^{•-}
6
7
8 or HO[•] [40]. Therefore, it is good capture probe for photoinduced electrons, as well as
9
10 indirect indication of hole⁺. Fig. 7c shows that TEMPO signal (g value ~ 2.000)
11
12 intensity reduced 14% after 5 min light illumination, and almost disappeared after 20
13
14 min illumination, suggesting the generation of electrons and hence holes⁺. Interestingly,
15
16
17 EPR measurements also demonstrate the involvement of oxygen vacancies, VO^{••}, in
18
19
20 PrO_x-catalyzed oxidation. Using DMPO as spin label, either using ABTS or TMB
21
22
23 substrate, Fig. 7d shows clear reduction of VO^{••} (g value ~ 2.003) signals when sodium
24
25
26 oxalate, the hole⁺ inhibitor, were added to the mixture. The oxidation of TMB over
27
28
29 PrO_x-C in dark and under day light (Fig. S7) have been studied. Results showed that
30
31
32 the enzymatic activity for oxidation of TMB is lower in the dark compared with under
33
34
35 day light, suggesting the possible influence of photo-induced hole⁺.
36
37
38
39
40
41
42
43
44
45
46
47
48
49
50
51
52
53
54
55
56
57
58
59
60
61
62
63
64
65

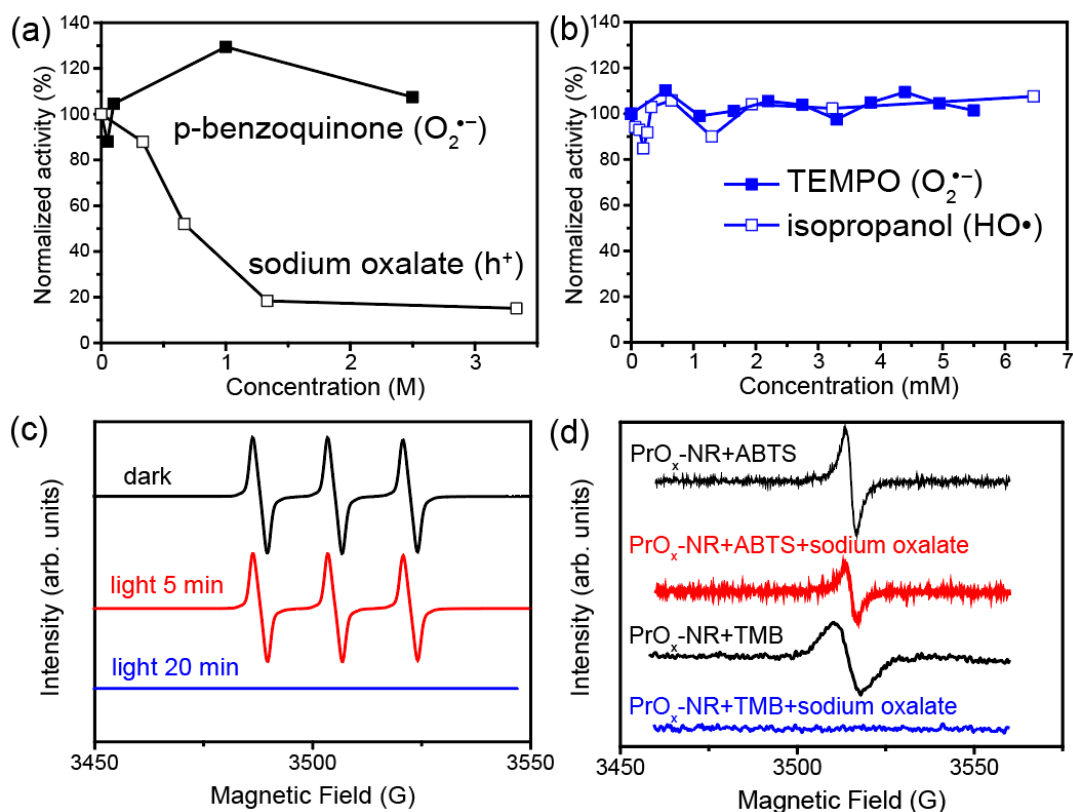


Fig. 7. (a) Normalized catalytic activity of PrO_x-NR oxidizing TMB after adding p-benzoquinone (O₂^{•-} scavenger) and sodium oxalate (hole⁺ scavenger). (b) Effect of isopropanol (HO• scavenger) and TEMPO (O₂^{•-} scavenger). (c) EPR spectra of spin label TEMPO for electrons generated by 3 mg/mL PrO_x-NR pH 4.0 in dark and after light illumination of 5 and 20 min. (d) EPR spectra of spin label DMPO for 3 mg/mL PrO_x-NR with 1 mM ABTS and 0.1 mM TMB before and after addition of 20 mM sodium oxalate.

Taken together, the above-mentioned results suggest that the catalytic oxidation, or the oxidase-like activity, of PrO_x is closely related to hole⁺ and VO^{••}. Energy level diagram (Fig. 8a) of PrO_x-NR demonstrates that the distance between O-2p Valence Band (VB) (2.81 eV) and Pr 4f Conduction Band (CB) is 2.06 eV, and VO^{••} is located between these two band gaps. The level of VO^{••} can be estimated from the photon energy profile (Fig. 8b) based on UV-Vis diffuse reflectance data in Fig. 4. Each absorption band can be associated with an electron transition between two energy states (Fig. 8a). For example, the absorption bands at 1.29 and 1.55 eV could be assigned to the charge transfer transition from oxygen vacancies to Pr 4f CB. Fig. 8c shows VB

XPS of $\text{PrO}_x\text{-NR}$ in comparison with a 100% reduced praseodymium oxide [3]. Their O-2p VB maximum are similar at around 2.81 eV.

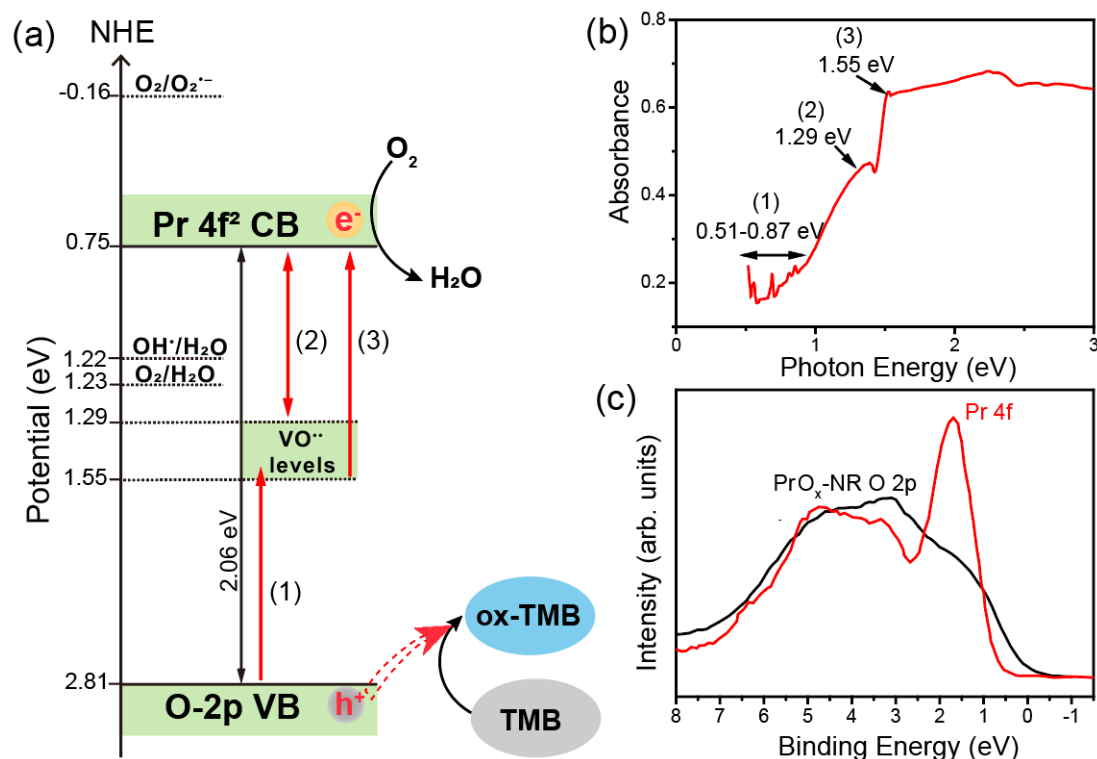


Fig. 8. (a) Energy level diagram and excitation process of $\text{PrO}_x\text{-NR}$. (b) Photon energy spectrum of $\text{PrO}_x\text{-NR}$. (c) Valence band XPS data for a 100% reduced praseodymium oxide and $\text{PrO}_x\text{-NR}$.

The mechanism for PrO_x -catalyzed oxidation is proposed to be initiated by electrons transferring from O-2p VB to the VO^{2+} band, leaving a hole⁺ available to oxidize substrates like TMB and DOPA (Fig. 8a). Meanwhile, the electron can be further transferred to the conduction band and O_2 , which is eventually reduced to H_2O . The formation of $\text{O}_2^{\bullet-}$ from O_2 requires the potential of electron to be less than -0.16 eV [40], while the standard reduction potential for the $\text{O}_2/\text{H}_2\text{O}$ couple is 1.23 V (Fig. 8a) [41]. It is likely that the electron can reduce O_2 to H_2O without generating $\text{O}_2^{\bullet-}$. On the other side, although hole⁺ has a greater potential (2.81 eV) than HO^\bullet (2.2 eV), the inhibition measurement (Fig. 7b) shows no presence of HO^\bullet radicals. Therefore, we

1 propose that hole⁺ may probably oxidize the substrate directly. Moreover, the presence
2
3 of VO^{••} and high oxygen mobility of PrO_x are able to facilitate the electron/hole⁺
4
5 separation, which leads to the high oxidizing capability of PrO_x catalyst.
6
7

8
9 Despite the proposed mechanism above, it is worth noting that the oxidase-like
10
11 property of PrO_x is probably not only the result of a single factor. The hole⁺ in PrO_x
12
13 crystalline lattice can be also generated by various oxidative species (HO•, O₂[•], etc),
14
15 directly or indirectly participating in the oxidation (depicted as dotted arrow in Fig. 8a).
16
17 For example, although the addition of HO• inhibitor (isopropanol) shows no impact on
18
19 the oxidase-like activity of PrO_x (Fig. 7b) at increasing concentration, fluorescent
20
21 experiments using HO• probe terephthalic acid (TA) indicate the presence of a small
22
23 amount of HO• radical compared with negative control without PrO_x-C and positive
24
25 control with PrO_x-C experiments (Fig. S8). The TA aqueous solution and a mixture of
26
27 TA and H₂O₂ solution do not show a fluorescent peak at 435 nm, which is a
28
29 characteristic peak of 2-hydroxy TA (TAOH) generated from reaction between HO•
30
31 radicals and TA. When PrO_x-C was mixed with TA, there is a small fluorescent peak at
32
33 435 nm. The addition of H₂O₂ to the mixture of PrO_x-C and TA generates more HO•
34
35 radicals, thus a stronger peak appears at 435 nm. All these results suggest that the
36
37 existence of multiple routes for generation of oxidative species, such as the interaction
38
39 of OH⁻ with hole⁺ to form HO• (OH⁻ + h⁺ → HO•). The origin of oxidase-like activity
40
41 of PrO_x in the crystalline lattice may be eventually related to the reversible exchange
42
43 between Pr³⁺ and Pr⁴⁺ which is associated with the formation and migration of oxygen
44
45 vacancies. Pr₆O₁₁ has the highest oxygen mobility among all rare earth oxides [7], partly
46
47
48
49
50
51
52
53
54
55
56
57
58
59
60
61
62
63
64
65

1 because of its inherent structure of naturally “doped” Pr³⁺ in Pr⁴⁺ stoichiometry. The
2
3 oxygen defects or vacancies, particularly abundant in PrO_x-NR of this study, lead to its
4
5 excellent oxygen storage capacity, which is fundamental for Pr₆O₁₁ in previous catalytic
6
7 studies [9].
8
9

10
11 PrO_x as oxidase is sensitive to reducing agents, such as L-cysteine. Absorbance
12
13 of oxidized TMB decreases with addition of L-cysteine (Fig. 9a). In fact, absorbance
14
15 change @652 nm decreases linearly with L-cysteine concentration within the 2×10⁻⁷ ~
16
17 1×10⁻⁵ M range, with a limit of detection (LOD) of 2.3×10⁻⁹ M (Fig. 9b). In comparison
18
19 with other nanomaterials employed in various L-cysteine sensors (Table S2) [42-44],
20
21 PrO_x-TMB platform appears to be a good colorimetric sensing probe for cysteine and
22
23 similarly structured Hcy in blood or serum samples, with negligible influence from salt
24
25 or amino acids of similar structures (Fig. 9c).
26
27
28
29
30
31
32

33
34 Oxidase activity of PrO_x-NR is also very sensitive to the fluoride anion (F⁻), a
35
36 high dose of which is toxic to human health and affects the aqueous conditions in the
37
38 environment [45]. As shown in Fig. 9d, F⁻ addition inhibits TMB oxidation over PrO_x-
39
40 NR and the inhibition level is in linear relationship to F⁻ concentration (Fig. 9e).
41
42 Meanwhile, other halides (Cl⁻ and Br⁻) and anions (SO₄²⁻, PO₄³⁻ and CO₃²⁻) do not
43
44 induce such dramatic effect (Fig. 9f). This high selectivity for F⁻ ions of PrO_x-TMB
45
46 system can be used as a sensing platform for the excessively harmful F⁻ anions which
47
48 could cause dental mottling and skeletal manifestation [46]. For example, this method
49
50 can be employed to measure the fluoride content in a supermarket toothpaste (Oral-B
51
52 as in Fig. 9d). To minimize the matrix effects, standard addition method was used (Fig.
53
54
55
56
57
58
59
60
61
62
63
64
65

S6) [16]. Accordingly, the measured F^- content is 0.14%, which is very close to the labelled value (0.15%) on the toothpaste, suggesting good accuracy and applicability of this method in ordinary F^- detection.

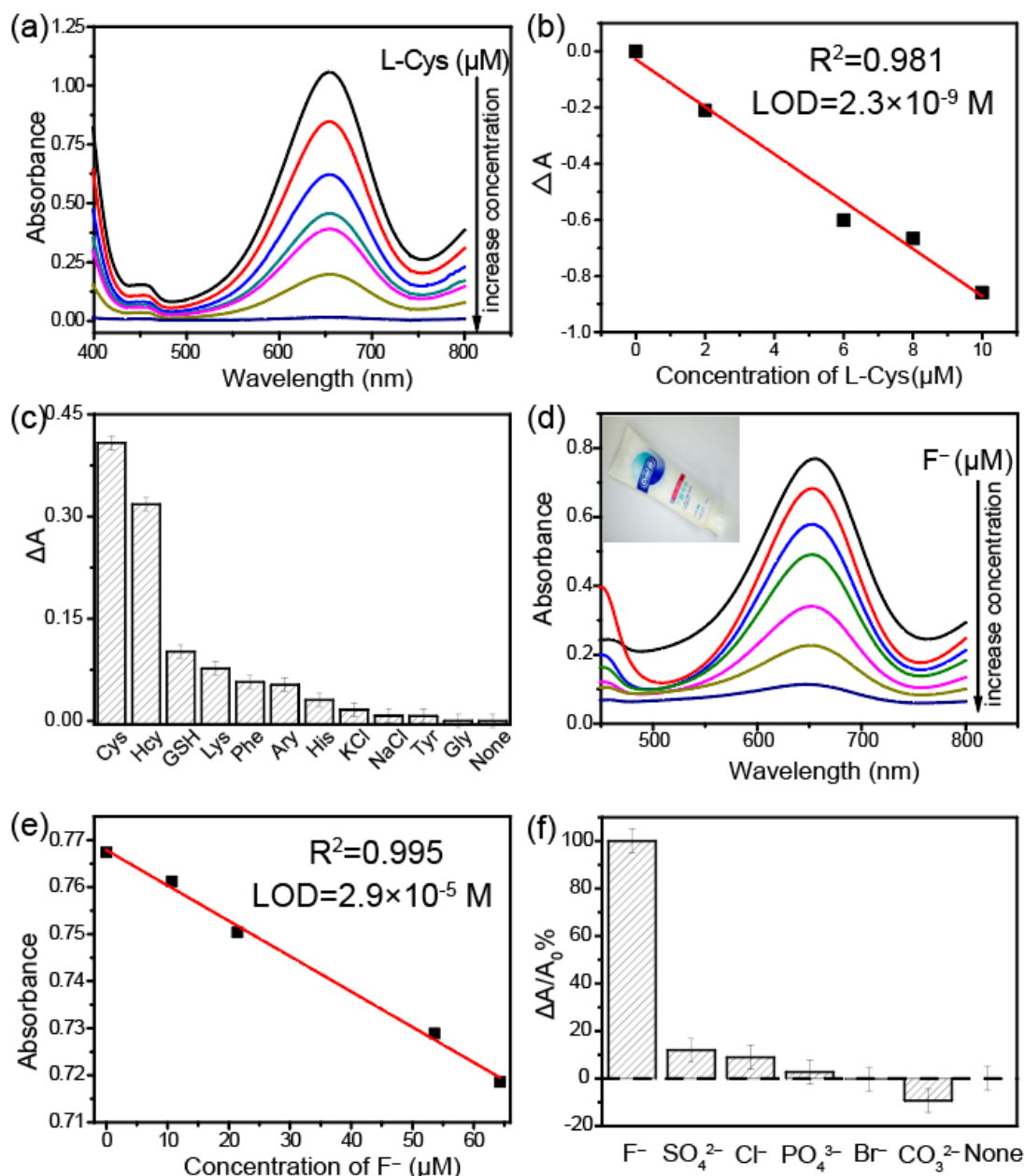


Fig. 9. (a) UV-Vis spectra of 0.2 mM TMB oxidized by 0.02 mg/mL PrO_x-NR in presence of L-cysteine (0 - 10 μM). (b) Correlation between $A_{652\text{ nm}}$ with L-cysteine concentration with LOD of $2.3 \times 10^{-9} M$ and $R^2 = 0.981$. (c) Selectivity of L-cysteine detection in comparison with salts and other amino acids. (d) UV-Vis spectra of 0.09 mM TMB oxidized by 0.1 mg/mL PrO_x-NR at different F^- concentration. Inset is picture of an Oral-B toothpaste containing 0.15%

1 fluoride. (e) Relationship between $A_{652\text{ nm}}$ with F^- concentration. (f) Selectivity of F^- detection
2 in comparison with other anions.

3
4 Another phenomenon worth noting is that the fluoride-induced inhibition on
5
6 PrO_x is in contrast with the enhancement effect of fluoride on the neighbor oxide CeO_2
7
8 ^[47]. Based on previous EPR and Raman studies ^[48, 49], F^- anions are adsorbed on surface
9
10 of CeO_2 , increasing the concentration of $VO^{\bullet\bullet}$, but does not affect the amount of
11
12 generated $O_2^{\bullet-}$ or HO^\bullet in function of mimicking oxidase. However, it can accelerate the
13
14 oxidation process by replacing the oxidation product quickly on CeO_2 surface. Oxidase-
15
16 like PrO_x also functions through $VO^{\bullet\bullet}$, but its interaction with F^- is different. Fig. 10
17
18 shows XPS spectra of PrO_x-C before and after mixing with F^- . Opposite to CeO_2 , whose
19
20 Ce^{3+} concentration increased significantly (from 38% to 45%) after F^- immersion ^{[48,}
21
22 ^{49]}, the percentage of Pr^{3+} on PrO_x decreases from 61% to 56%, while the ratio of
23
24 $O_{\text{carbonate}}/O_{\text{lattice}}$ decreases from 1.9 to 1.45. Adsorption of F element is also confirmed on
25
26 PrO_x surface because a new F *1s* peak at 684 eV appears in XPS of F^- -treated PrO_x (Fig.
27
28 S9) ^[50]. F^- was reported to bind to hydroxyl groups on surface of metal oxides including
29
30 Mg-Al ^[50]. As a strong electron withdrawing ligand, the addition of F^- anions leads to
31
32 oxidation of some Pr^{3+} to Pr^{4+} in order to keep the charge balance in PrO_x . Thus, the
33
34 active sites Pr^{3+} on PrO_x surface decrease and fluoride-induced inhibition occurs.
35
36 Secondly, F^- may interrupt the electron transfer pathway and reduce the formation of
37
38 surface hole⁺, which also causes the inhibition of PrO_x activity. These are probably the
39
40 reasons why F^- has very opposite effect on the oxidase-like activity of PrO_x to CeO_2 .
41
42
43
44
45
46
47
48
49
50
51
52
53
54
55
56
57
58
59
60
61
62
63
64
65

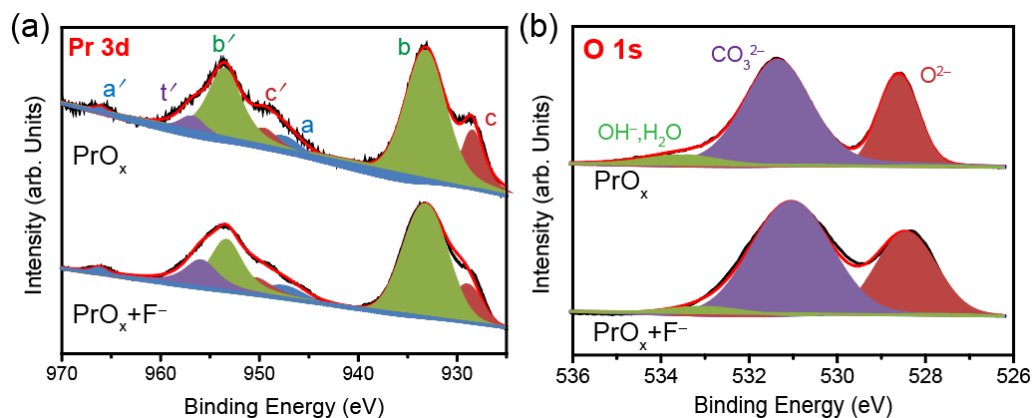


Fig. 10. XPS spectra of (a) Pr 3d and (b) O 1s of PrO_x-C before and after treating with 10 mM F⁻ solution.

Fig. 11 illustrates schematically the possible mechanism in the multi-functional oxidase-like activity of PrO_x. Praseodymium cations can exist with +3 and +4 valence states in PrO_x samples. PrO_x has the highest oxygen mobility because it has a larger number of possible phases for the oxides, so that the variety of stable phases enable fast changes in the oxidation states of praseodymium. PrO_x demonstrates high multi-oxidase activities which can be specifically tuned by its morphology, size, redox property, Pr³⁺/Pr⁴⁺ ratio and reducing inhibitor such as L-cysteine. Due to the generated hole⁺, oxygen vacancies and high oxygen mobility, PrO_x-NR is able to initiate the oxidation and polymerization of DOPA in acidic condition. Moreover, adsorption of F⁻ can inhibit the activity of PrO_x-NR, which conversely enables the linear detection of F⁻. This effect makes PrO_x a good probe for F⁻ sensing, but with completely different mechanism to CeO₂ which detects F⁻ by the boosted activity. In an environment of weak target presence, it is usually easier to detect reduction of a strong signal (signal-off) than enhancement of a weak signal (signal-on) with possibly high background noise. From this point of view, for F⁻ detection normally at low concentrations in most testing environments, PrO_x-NR is probably better than CeO₂ nanomaterials as sensors.

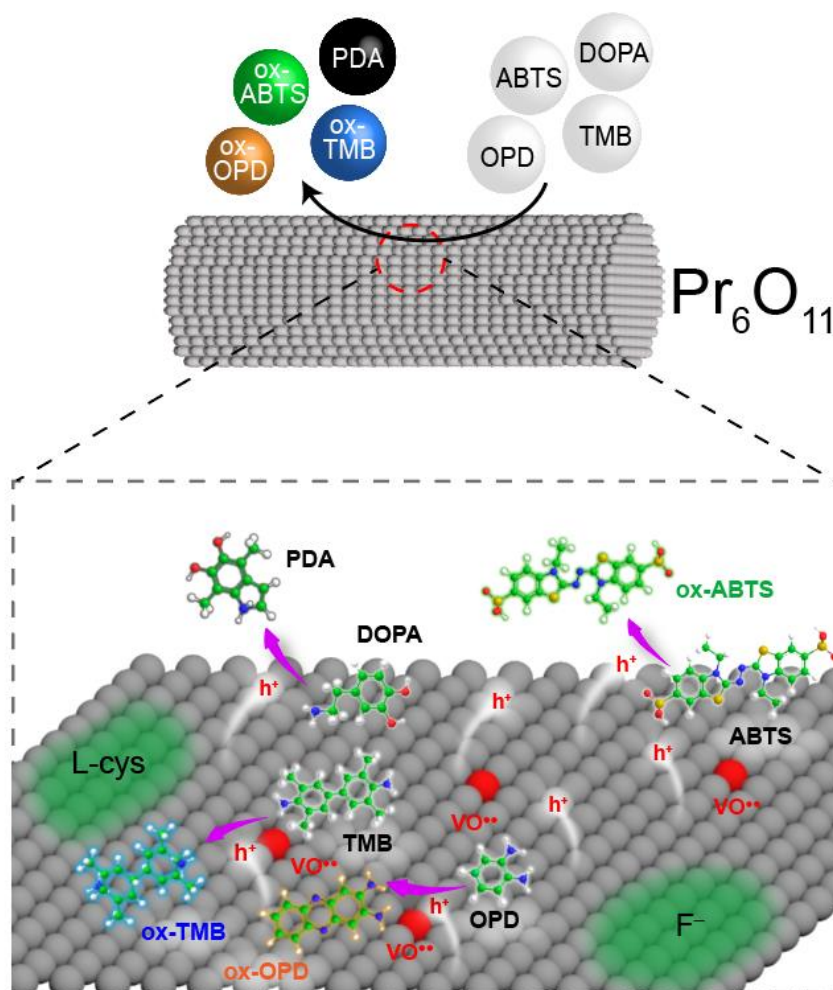


Fig. 11. Schematic illustration of how PrO_x-NR catalyzes the oxidation of several substrates including TMB, ABTS, OPD and DOPA. The oxidizing activity is high enough to oxidize and polymerize DOPA into PDA in acidic conditions. The key intermediates and reactive species are hole⁺ and oxygen vacancies VO²⁺, instead of O₂⁻ or HO[•], in the oxidation process.

4. Conclusions

PrO_x is firstly reported to exhibit multi-functional oxidase-like activities with significantly high kinetic performance. Three types of PrO_x samples with different morphologies and surface areas are compared in their catalytic activities of oxidizing a series of amino and polyphenol substrates, such as TMB, ABTS, OPD and DOPA. The polymerization of DOPA can be triggered by PrO_x-NR under acidic condition to produce polydopamine, a highly useful wet bioadhesive. Different from previously

1 reported oxidase-like nanozymes, hole⁺ and oxygen vacancies may play important roles
2
3 in the oxidation process by PrO_x. Adsorption of F⁻ on PrO_x inhibits its activity, in clear
4
5 contrast to CeO₂, probably because of the increased concentration of Pr⁴⁺ on surface
6
7 and reduced oxygen accessibility by the F⁻ blockage. These results not only shed some
8
9 light on the discovery of REO artificial enzymes with new mechanism, but also imply
10
11 a new sensor for F⁻ detection in fields of contamination and overdose.
12
13
14
15
16
17
18
19

20 **CRedit authorship contribution statement**

21
22 **Lei Jiang:** Conceptualization, Investigation, Validation, Data curation, Writing
23
24 – original draft, Methodology, Formal analysis, Writing – review & editing. **Yaning**
25
26 **Han:** Data curation, Formal analysis. **Susana Fernández-García:** Investigation,
27
28 Review & editing. **Miguel Tinoco:** Investigation, Review & editing. **Zhuang Li:**
29
30 Investigation. **Pengli Nan:** Investigation. **Jingtao Sun:** Investigation. **Juan J.**
31
32 **Delgado:** Investigation, Methodology, Review & editing, Funding acquisition, Project
33
34 administration. **Huiyan Pan:** Investigation. **Ginesa Blanco:** Investigation, Review &
35
36 editing. **Javier Martínez-López:** Investigation. **Ana B. Hungría:** Supervision, Review
37
38 & editing. **Jose J. Calvino:** Supervision, Review & editing. **Xiaowei Chen:**
39
40 Conceptualization, Methodology, Investigation, Funding acquisition, Project
41
42 administration, Resources, Supervision, Data curation, Writing – review & editing.
43
44
45
46
47
48
49
50
51
52
53
54
55

56 **Declaration of Competing Interest**

57
58 The authors declare that they have no known competing financial interests or
59
60
61
62
63
64
65

1 personal relationships that could have appeared to influence the work reported in this
2
3 paper.
4
5
6
7

8 **Acknowledgements**

10 This work has been supported by the Ministry of Science, Innovation and
11
12 Universities of Spain with reference number of PID2020-113809RB-C33 and Junta de
13
14 Andalucía (Spain) with reference number of PY18-2727. This work has been co-
15
16 financed by the 2014-2020 ERDF Operational Program and by the Department of
17
18 Economy, Knowledge, Business and University of the Regional Government of
19
20 Andalusia with project reference FEDER-UCA18-107316. The research projects
21
22 funded by Natural Science Foundation of Shandong Province (ZR2017LB028), Key
23
24 R&D Program of Shandong Province (2018GSF118032), and Fundamental Research
25
26 Funds for the Central Universities (18CX02125A) in China are also acknowledged. M.
27
28 Tinoco thanks FPU scholarship program from Ministry of Science and Innovation of
29
30 Spain. H. Pan is grateful for financial support from Chinese Scholarship Council to
31
32 accomplish her PhD study in University of Cadiz (Spain). TEM/STEM data were
33
34 acquired at the DME-UCA node of the Unique Spanish Infrastructure for Electron
35
36 Microscopy of Materials (ICTS-ELECMI).
37
38
39
40
41
42
43
44
45
46
47
48
49
50
51

52 **References**

- 53 [1] Q. Liu, A. Zhang, R. Wang, Q. Zhang, D. Cui, A review on metal- and metal
54 oxide-based nanozymes: Properties, mechanisms, and applications,
55 Nanomicro Lett. 13 (2021) 1-53. [https://dx.doi.org/10.1007/s40820-021-](https://dx.doi.org/10.1007/s40820-021-00674-8)
56 [00674-8](https://dx.doi.org/10.1007/s40820-021-00674-8).
57
58 [2] Y. Chong, Q. Liu, C. Ge, Advances in oxidase-mimicking nanozymes:
59
60
61
62
63
64
65

- Classification, activity regulation and biomedical applications, *Nano Today*. 37 (2021) 101076. <https://dx.doi.org/10.1016/j.nantod.2021.101076>.
- [3] L. Jiang, S. Fernandez-Garcia, M. Tinoco, Z. Yan, Q. Xue, G. Blanco, J. J. Calvino, A. B. Hungria, X. Chen, Improved oxidase mimetic activity by praseodymium incorporation into ceria nanocubes, *ACS Appl. Mater. Interfaces*. 9 (22) (2017) 18595-18608. <https://dx.doi.org/10.1021/acsami.7b05036>.
- [4] Z. Chen, Z. Huang, Y. Sun, Z. Xu, J. Liu, The most active oxidase-mimicking Mn₂O₃ nanozyme for biosensor signal generation, *Chem. Eur. J.* 27 (2021) 9597-9604. <https://dx.doi.org/10.1002/chem.202100567>.
- [5] A. Schaefer, S. Gevers, V. Zielasek, T. Schroeder, J. Falta, J. Wollschläger, M. Bäumer, Photoemission study of praseodymia in its highest oxidation state: The necessity of in situ plasma treatment, *J. Chem. Phys.* 134 (2011) 0-7. <https://dx.doi.org/10.1063/1.3516953>.
- [6] Z.C. Kang, Lanthanide higher oxides: The contributions of Leroy Eyring, *Handbook on the Physics and Chemistry of Rare Earths*. 38 (2008) 1-53. [https://dx.doi.org/10.1016/S0168-1273\(07\)38001-X](https://dx.doi.org/10.1016/S0168-1273(07)38001-X).
- [7] N. Krishna Chandar, R. Jayavel. Structural, morphological and optical properties of solvothermally synthesized Pr(OH)₃ nanoparticles and calcined Pr₆O₁₁ nanorods, *Mater. Res. Bull.* 50 (2014) 417-420. <https://dx.doi.org/10.1016/j.materresbull.2013.11.006>.
- [8] M.F. Luo, Z.L. Yan, L.Y. Jin, Structure and redox properties of Ce_xPr_{1-x}O_{2-δ} mixed oxides and their catalytic activities for CO, CH₃OH and CH₄ combustion, *J. Mol. Catal. A-Chem.* 260 (1-2) (2006) 157-162. <https://dx.doi.org/10.1016/j.molcata.2006.07.012>.
- [9] V. Alcalde-Santiago, E. Bailón-García, A. Davó-Quñonero, D. Lozano-Castelló, A. Bueno-López, Three-dimensionally ordered macroporous PrO_x: An improved alternative to ceria catalysts for soot combustion, *Appl. Catal. B*. 248 (2019) 567-572. <https://dx.doi.org/10.1016/j.apcatb.2018.10.049>.
- [10] L. Jiang, M. Tinoco, S. Fernández-García, Y. Sun, M. Traviankina, P. Nan, Q. Xue, H. Pan, A. Aguinaco, J. M. González-Leal, G. Blanco, E. Blanco, A. B. Hungría, J. J. Calvino, X. Chen, Enhanced artificial enzyme activities on the reconstructed sawtoothlike nanofacets of pure and Pr-doped ceria nanocubes, *ACS Appl. Mater. Interfaces*. 13 (2021) 38061-38073. <https://dx.doi.org/10.1021/acsami.1c09992>.
- [11] L. Jiang, J. Zhong, Y. Li, H. Liu, S. Zhang, X. Zhu, Z. Liu, Y. Chen, S. Fernandez-Garcia, X. Chen, Coordination of H₂O₂ on praseodymia nanorods and its application in sensing cholesterol, *J. Sci-Adv. Mater. Dev.* 7 (2) (2022) 100443. <https://dx.doi.org/10.1016/j.jsamd.2022.100443>.
- [12] J.G. Kang, B.K. Min, Y. Sohn, Physicochemical properties of praseodymium hydroxide and oxide nanorods, *J. Alloys Compd.* 619 (2015) 165-171. <https://dx.doi.org/10.1016/j.jallcom.2014.09.059>.
- [13] L. Ma, W.X. Chen, J. Zhao, Y. Zheng, Synthesis of Pr(OH)₃ and Pr₆O₁₁ nanorods by microwave-assisted method: Effects of concentration of alkali

- and microwave heating time, *J. Cryst. Growth.* 303 (2) (2007) 590-596.
<https://dx.doi.org/10.1016/j.jcrysgro.2006.12.035>.
- [14] L. Jiang, Y. Han, Y. Li, Z. Li, S. Zhang, X. Zhu, Z. Liu, Y. Chen, S. Fernandez-Garcia, Y. Tang, X. Chen, Split-type assay for wide-range sensitive sensing of Ochratoxin A with praseodymia nanorods, *Colloids Surf. A Physicochem. Eng. Asp.* 652 (5) (2022) 129804.
<https://dx.doi.org/10.1016/j.colsurfa.2022.129804>.
- [15] X. Li, Y. Dong, X. Liu, L. Li, Y. Gao, Z. Cao, J. Liu, Catalytic action of rare earth oxide (La₂O₃, CeO₂, Pr₆O₁₁) on electrochemical oxidation of activated carbon in molten KOH–NaOH, *J. Rare Earth.* 40 (7) (2022) 1083-1090.
<https://dx.doi.org/10.1016/j.jre.2021.07.002>.
- [16] M. Wiczorek, S. Rengevicova, P. Świt, A. Woźniakiewicz, J. Kozak, P. Kościelniak, New approach to H-point standard addition method for detection and elimination of unspecific interferences in samples with unknown matrix, *Talanta*, 170 (2017) 165-172. <https://dx.doi.org/10.1016/j.talanta.2017.03.101>.
- [17] M.Y. Sinev, G.W. Graham, L.P. Haack, M. Shelef, Kinetic and structural studies of oxygen availability of the mixed oxides Pr_{1-x}M_xO_y (M = Ce, Zr), *J. Mater. Res.* 11 (1996) 1960-1971. <https://dx.doi.org/10.1557/jmr.1996.0247>.
- [18] H. Borchert, Y.V. Frolova, V.V. Kaichev, I. P. Prosvirin, G. M. Alikina, A. I. Lukashovich, V. I. Zaikovskii, E. M. Moroz, S. N. Trukhan, V. P. Ivanov, E. A. Paukshtis, V. I. Bukhtiyarov, V. A. Sadykov, Electronic and chemical properties of nanostructured cerium dioxide doped with praseodymium, *J. Phys. Chem. B.* 109 (12) (2005) 5728-38.
<https://dx.doi.org/10.1021/jp045828c>.
- [19] E. Poggio-Fraccari, G. Baronetti, F. Mariño, Pr³⁺ surface fraction in CePr mixed oxides determined by XPS analysis, *J. Electron Spectros. Relat. Phenomena.* 222 (2018) 1-4. <https://dx.doi.org/10.1016/j.elspec.2017.11.003>.
- [20] S. Bernal, G. Blanco, J.M. Gatica, J. A. Pérez-Omil, J. M. Pintado, H. Vidal, Chemical reactivity of binary rare earth oxides, in: G. Adachi, N. Imanaka, Z.C. Kang, (Eds.), *Binary Rare Earth Oxides*, Kluwer Academic Publishers, Dordrecht, 2004, pp. 9-55.
- [21] S. Bernal, F.J. Botana, G. Cifredo, J. J. Calvino, A. Jobacho, J. M. Rodriguez-Izquierdoet, Preparation and characterization of a praseodymium oxide to be used as a catalytic support, *J. Alloys. Compd.* 180 (1-2) (1992) 271-279.
[https://dx.doi.org/10.1016/0925-8388\(92\)90392-m](https://dx.doi.org/10.1016/0925-8388(92)90392-m).
- [22] A.M. D'Angelo, A.L. Chaffee, Correlations between oxygen uptake and vacancy concentration in Pr-doped CeO₂, *ACS Omega*, 2 (6) (2017) 2544-2551. <https://dx.doi.org/10.1021/acsomega.7b00550>.
- [23] C.I. Silva Filho, A.L. Oliveira, S.C.F. Pereira, Gilberto F. de Sá, L. L. da Luz, S. Alves, Júnior, Bright thermal (blackbody) emission of visible light from LnO₂ (Ln = Pr, Tb), photoinduced by a NIR 980 nm laser, *Dalton Trans.* 48 (2019) 2574-2581. <https://dx.doi.org/10.1039/c8dt04649b>.
- [24] A.G. Shende, S.G. Ghugal, D. Vidyasagar, S. B.Kokane, Jagannath, S. S. Umare, R. Sasikala, Solvent free solid-state synthesis of Pr₆O₁₁/g-C₃N₄ visible

- light active photocatalyst for degradation of av7 dye, *Mater. Res. Bull.* 107 (2018) 154-163. <https://dx.doi.org/10.1016/j.materresbull.2018.07.022>.
- [25] T. Xia, X. Chen, Revealing the structural properties of hydrogenated black TiO₂ nanocrystals, *J. Mater. Chem. A*. 1 (2013) 2983-2989. <https://dx.doi.org/10.1039/c3ta01589k>.
- [26] P.X. Huang, F. Wu, B.L. Zhu, G. R. Li, Y. L. Wang, X. P. Gao, H. Y. Zhu, T. Y. Yan, W. P. Huang, S. M. Zhang, D. Y. Song, Praseodymium hydroxide and oxide nanorods and Au/Pr₆O₁₁ nanorod catalysts for CO oxidation, *J. Phys. Chem. B*. 110 (4) (2006) 1614-1620. <https://dx.doi.org/10.1021/jp055622r>.
- [27] B. Liu, J. Liu, Accelerating peroxidase mimicking nanozymes using DNA, *Nanoscale*. 7 (33) (2015) 13831-13835. <https://dx.doi.org/10.1039/c5nr04176g>.
- [28] S. Fernandez-Garcia, L. Jiang, M. Tinoco, A.B. Hungria, J. Han, G. Blanco, J.J. Calvino, X. Chen, Enhanced hydroxyl radical scavenging activity by doping lanthanum in ceria nanocubes, *J. Phys. Chem. C*. 120 (3) (2016) 1891-1901. <https://dx.doi.org/10.1021/acs.jpcc.5b09495>.
- [29] F. Ghorbani, A. Zamanian, A. Behnamghader, M. D. Joupari, A facile method to synthesize mussel-inspired polydopamine nanospheres as an active template for in situ formation of biomimetic hydroxyapatite, *Mater. Sci. Eng. C Mater. Biol. Appl.* 94 (2019) 729-739. <https://dx.doi.org/10.1016/j.msec.2018.10.010>.
- [30] Y. Mao, M. Zhu, W. Wang, D. Yu, Well-defined silver conductive pattern fabricated on polyester fabric by screen printing a dopamine surface modifier followed by electroless plating, *Soft Matter*. 14 (7) (2018) 1260-1269. <https://dx.doi.org/10.1039/c7sm02246h>.
- [31] X. Du, L. Li, J. Li, C. Yang, N. Frenkel, A. Welle, S. Heissler, A. Nefedov, M. Grunze, P. A. Levkin, UV-triggered dopamine polymerization: Control of polymerization, surface coating, and photopatterning, *Adv. Mater.* 26 (2014) 8029-8033. <https://dx.doi.org/10.1002/adma.201403709>.
- [32] J.E. Lemaster, A.S. Jeevarathinam, A. Kumar, B. Chandrasekar, F. Chen, J. V. Jokerst, Synthesis of ultrasmall synthetic melanin nanoparticles by UV irradiation in acidic and neutral conditions, *ACS Appl. Bio Mater.* 2 (2019) 4667-4674. <https://dx.doi.org/10.1021/acsabm.9b00747>.
- [33] T.P. Chen, T. Liu, T.L. Su, J. Liang, Self-polymerization of dopamine in acidic environments without oxygen, *Langmuir*. 33 (2017) 5863-5871. <https://dx.doi.org/10.1021/acs.langmuir.7b01127>.
- [34] W. Zheng, H. Fan, L. Wang, Z. Jin, Oxidative self-polymerization of dopamine in an acidic environment, *Langmuir*. 31 (2015) 11671-11677. <https://dx.doi.org/10.1021/acs.langmuir.5b02757>.
- [35] M. Zhu, J. Lu, Y. Hu, Y. Liu, S. Hu, C. Zhu, Photochemical reactions between 1,4-benzoquinone and O₂^{•-}, *Environ. Sci. Pollut. Res.* 27 (2020) 31289-31299. <https://dx.doi.org/10.1007/s11356-020-09422-8>.
- [36] X. Ma, H. Hao, W. Sheng, F. Huang, X. Lang, Bridging green light photocatalysis over hierarchical Nb₂O₅ for the selective aerobic oxidation of sulfides, *J. Mater. Chem. A*. 9 (2021) 2214-2222.

- <https://dx.doi.org/10.1039/d0ta10757c>.
- [37] Q. Zhao, Q. Fang, H. Liu, Y. Li, H. Cui, B. Zhang, S. Tian, Halide-specific enhancement of photodegradation for sulfadiazine in estuarine waters: Roles of halogen radicals and main water constituents, *Water Res.* 160 (2019) 209-216. <https://dx.doi.org/10.1016/j.watres.2019.05.061>.
- [38] N.A. Lima, G.C. Mendonça, G.T.S.T. da Silva, B. S. de Lima, E. C. Paris, M. I. B. Bernardi, Influence of the synthesis method on CuWO₄ nanoparticles for photocatalytic application, *J. Mater. Sci. Mater. Electron.* 32 (2021) 1139-1149. <https://dx.doi.org/10.1007/s10854-020-04887-2>.
- [39] D. Wu, S. Yue, W. Wang, T. An, G. Li, H. Y. Yip, H. Zhao, P. K. Wong, Boron doped BiOBr nanosheets with enhanced photocatalytic inactivation of escherichia coli, *Appl. Catal. B.* 192 (2016) 35-45. <https://dx.doi.org/10.1016/j.apcatb.2016.03.046>.
- [40] W. He, H. Jia, W.G. Wamer, Z. Zheng, P. Li, J. H. Callahan, J. Yin, Predicting and identifying reactive oxygen species and electrons for photocatalytic metal sulfide micro-nano structures, *J. Catal.* 320 (2014) 97-105. <https://dx.doi.org/10.1016/j.jcat.2014.10.004>.
- [41] J.A. Herron, J. Kim, A.A. Upadhye, G. W. Huber, C. T. Maravelias, A general framework for the assessment of solar fuel technologies, *Energy Environ. Sci.* 8 (2015) 126-157. <https://dx.doi.org/10.1039/c4ee01958j>.
- [42] T. Matsunaga, T. Kondo, I. Shitanda, Y. Hoshi, M. Itagaki, T. Tojo, M. Yuasa, Sensitive electrochemical detection of L-cysteine at a screen-printed diamond electrode, *Carbon.* 173 (2021) 395-402. <https://dx.doi.org/10.1016/j.carbon.2020.10.096>.
- [43] S. Hashmi, M. Singh, P. Weerathunge, E. L. H. Mayes, P. D. Mariathomas, S. N. Prasad, R. Ramanathan, V. Bansal, Cobalt sulfide nanosheets as peroxidase mimics for colorimetric detection of L-cysteine, *ACS Appl. Nano Mater.* 4 (2021) 13352-13362. <https://dx.doi.org/10.1021/acsanm.1c02851>
- [44] R. Prasetia, S. Fuangswasdi, F. Unob. Silver nanoparticle-supported hydroxyapatite as a material for visual detection of urinary cysteine, *Anal. Methods.* 11 (2019) 2888-2894. <https://dx.doi.org/10.1039/c9ay00725c>
- [45] A. Bhatnagar, E. Kumar, M. Sillanpää. Fluoride removal from water by adsorption-a review, *Chem. Eng. J.* 171 (2011) 811-840. <https://dx.doi.org/10.1016/j.cej.2011.05.028>.
- [46] O. Barbier, L. Arreola-Mendoza, L.M. Del Razo, Molecular mechanisms of fluoride toxicity, *Chem-Biol. Interact.* 188 (2010) 319-333. <https://dx.doi.org/10.1016/j.cbi.2010.07.011>.
- [47] B. Liu, Z. Huang, J. Liu, Boosting the oxidase mimicking activity of nanoceria by fluoride capping: Rivaling protein enzymes and ultrasensitive F(-) detection, *Nanoscale.* 8 (28) (2016) 13562-7. <https://dx.doi.org/10.1039/c6nr02730j>.
- [48] Y. Wang, T. Liu, J. Liu, Synergistically boosted degradation of organic dyes by CeO₂ nanoparticles with fluoride at low pH, *ACS Appl. Nano Mater.* 3 (2020) 842-849. <https://dx.doi.org/10.1021/acsanm.9b02356>.

- 1
2
3
4
5
6
7
8
9
10
11
12
13
14
15
16
17
18
19
20
21
22
23
24
25
26
27
28
29
30
31
32
33
34
35
36
37
38
39
40
41
42
43
44
45
46
47
48
49
50
51
52
53
54
55
56
57
58
59
60
61
62
63
64
65
- [49] Y. Zhao, Y. Wang, A. Mathur, Y. Wang, V. Maheshwari, H. Su, J. Liu, Fluoride-capped nanoceria as a highly efficient oxidase-mimicking nanozyme: Inhibiting product adsorption and increasing oxygen vacancies, *Nanoscale*. 11 (2019) 17841-17850. <https://dx.doi.org/10.1039/c9nr05346h>.
- [50] J. Liu, P. Zhao, Y. Xu, X. Jia, Mg-Al mixed oxide adsorbent synthesized using FCT template for fluoride removal from drinking water, *Bioinorg. Chem. Appl.* 2019 (3) (2019) 1-11. <https://dx.doi.org/10.1155/2019/5840205>.